

**SINGLE CRYSTAL GROWTH AND STUDY OF MAGNETIC
PROPERTIES OF THE ONE DIMENSIONAL SYSTEMS
 $\text{BaCu}_2\text{V}_2\text{O}_8$ AND $\text{Ba}(\text{Cu}_{1-x}\text{Zn}_x)_2\text{V}_2\text{O}_8$**

YUVAL SHILON

**A THESIS SUBMITTED IN PARTIAL FULFILLMENT
OF THE REQUIREMENTS FOR THE DEGREE OF
MASTER OF SCIENCE (PHYSICS)
FACULTY OF GRADUATE STUDIES
MAHIDOL UNIVERSITY
2015**

COPYRIGHT OF MAHIDOL UNIVERSITY

Thesis
entitled
**SINGLE CRYSTAL GROWTH AND STUDY OF MAGNETIC
PROPERTIES OF THE ONE DIMENSIONAL SYSTEMS
BaCu₂V₂O₈ AND Ba(Cu_{1-x}Zn_x)₂V₂O₈**

.....
Mr. Yuval Shilon
Candidate

.....
Asst. Prof. Kittiwit Matan,
Ph.D. (Physics)
Major advisor

.....
Lect. Sujin Suwanna,
Ph.D. (Mathematical Physics)
Co-advisor

.....
Lect. Yodchay Jompol,
Ph.D. (Physics)
Co-advisor

.....
Asst. Prof. Auemphorn Mutchimwong,
Ph.D. (Air Quality Assessment)
Acting Dean
Faculty of Graduate Studies
Mahidol University

.....
Assoc. Prof. Weerachai Siripunvaraporn,
Ph.D. (Geophysics)
Program Director
Doctor of Philosophy Program in
Physics
Faculty of Science, Mahidol University

Thesis
entitled
**SINGLE CRYSTAL GROWTH AND STUDY OF MAGNETIC
PROPERTIES OF THE ONE DIMENSIONAL SYSTEMS
BaCu₂V₂O₈ AND Ba(Cu_{1-x}Zn_x)₂V₂O₈**

was submitted to the Faculty of Graduate Studies, Mahidol University
for the degree of Master of Science (Physics)

on
July 15, 2015

.....
Mr. Yuval Shilon
Candidate

.....
Assoc. Prof. Chitnarong Sirisathitkul,
Ph.D. (Physics),
Chair

.....
Asst. Prof. Kittiwit Matan,
Ph.D. (Physics)
Member

.....
Lect. Yodchay Jompol,
Ph.D. (Physics)
Member

.....
Lect. Sujin Suwanna,
Ph.D. (Mathematical Physics)
Member

.....
Asst. Prof. Auemphorn Mutchimwong,
Ph.D. (Air Quality Assessment)
Acting Dean
Faculty of Graduate Studies
Mahidol University

.....
Prof. Skorn Mongkolsuk,
Ph.D. (Biological Science)
Dean
Faculty of Science
Mahidol University

ACKNOWLEDGEMENTS

The success of this thesis can be attributed to the attentive support from my Major advisor, Dr Kittiwit Matan, and co-advisors Dr. Yodchay Jompol and Dr. Sujin Suwanna. My special appreciation is extended to Dr. Taku J. Sato at Tohoku University, Japan, for the SQUID measurements and useful discussion.

I am grateful to Mr. Ganatee Gitgeatpong for his help and support throughout the course of my study at Mahidol.

I would like to thank the department of science, Mahidol University and Thailand Center of Excellence in Physics (ThEP), for their financial support and scholarship.

Finally, I would like to express my gratitude to my parents for their encouragement and support.

Yuval Shilon

SINGLE CRYSTAL GROWTH AND STUDY OF MAGNETIC PROPERTIES OF
THE ONE DIMENSIONAL SYSTEMS $\text{BaCu}_2\text{V}_2\text{O}_8$ AND $\text{Ba}(\text{Cu}_{1-x}\text{Zn}_x)_2\text{V}_2\text{O}_8$

YUVAL SHILON 5536410 SCPY/M

M.Sc. (PHYSICS)

THESIS ADVISORY COMMITTEE: KITTIWIT MATAN, Ph.D., SUJIN
SUWANNA, Ph.D., YODCHAY JOMPOL, Ph.D.

ABSTRACT

Polycrystalline samples of the quasi-one-dimensional, spin 1/2 chain compound $\text{BaCu}_2\text{V}_2\text{O}_8$ and the zinc doped $\text{Ba}(\text{Cu}_{1-x}\text{Zn}_x)_2\text{V}_2\text{O}_8$ ($x = 0.05, 0.1, 0.15, 0.2, 0.3$ and 0.4), were synthesized using the solid state reaction method. Small size single crystals ($\sim 1.5\text{mm}^3$) were grown using the vertical Bridgman-Stockbarger method and the slow cooling method. Crystal structure and magnetic properties were characterized using powder x-ray diffraction and superconducting Quantum Interference Device (SQUID), respectively. Magnetic susceptibility measurements on the polycrystalline samples suggested that the magnetic behavior of this compound was best described by an isolated dimer model. The effect of substituting zinc for copper on the spin gap (Δ) showed that Δ was weakly dependent on x , which confirmed that the isolated dimer model was valid in order to explain the origin of the spin gap in this system.

KEY WORDS: $\text{BaCu}_2\text{V}_2\text{O}_8$ / CRYSTAL GROWTH / SPIN GAP /
ONE DIMENSIONAL / SPIN 1/2 CHAIN

70 pages

CONTENTS

	Page
ACKNOWLEDGEMENTS	iii
ABSTRACT	iv
LIST OF TABLES	viii
LIST OF FIGURES	ix
CHAPTER I INTRODUCTION	1
1.1 Spin Exchange	1
1.2 One dimensional magnetism	2
1.3 Heisenberg model	4
1.3.1 XXZ model	5
1.3.2 Alternating exchange in the $S = 1/2$ spin chain	6
1.3.3 Isolated dimer model	7
1.4 Magnetization plateau	8
1.5 Thermodynamic properties of the Heisenberg $S = 1/2$ chain	8
CHAPTER II EXPERIMENTAL METHODS	11
2.1 Introduction	11
2.2 X-ray diffraction	11
2.2.1 Instruments	12
2.2.2 Data analysis	13
2.3 SQUID	14
2.3.1 Instruments	15
2.4 Neutron scattering	18
CHAPTER III LITERATURE REVIEW	20
3.1 Crystal structure of $\text{BaCu}_2\text{V}_2\text{O}_8$	20
3.2 Theoretical Model	20

CONTENTS(cont.)

	Page
3.3 Experimental results	22
3.3.1 Zinc doped $\text{BaCu}_{2-x}\text{Zn}_x\text{V}_2\text{O}_8$	24
3.4 Crystal growth	25
3.5 Motivation	26
CHAPTER IV SAMPLE PREPARATION AND	27
CHARACTERIZATION	
4.1 Polycrystalline $\text{BaCu}_2\text{V}_2\text{O}_8$	27
4.2 Sample characterization	30
4.3 Crystal growth of $\text{BaCu}_2\text{V}_2\text{O}_8$	37
4.3.1 The slow cooling method	37
4.3.2 The Bridgman-Stockbarger method	38
4.3.2.1 Furnace settings	39
CHAPTER V SUSCEPTIBILITY MEASUREMENT	42
5.1 Susceptibility measurement	42
5.1.1 Sample preparation	42
5.1.2 Measurement process	43
5.2 Measurement results	44
5.3 Data analysis	49
5.3.1 Fit to the alternating chain model	54
CHAPTER VI DISCUSSION	57
6.1 Sample preparation	57
6.2 Magnetic susceptibility of $\text{BaCu}_2\text{V}_2\text{O}_8$	58
6.3 Magnetic susceptibility of zinc doped $\text{Ba}(\text{Cu}_{1-x}\text{Zn}_x)_2\text{V}_2\text{O}_8$	59
6.4 Conclusion	61
CHAPTER VII SUGGESTIONS	64
7.1 Inelastic neutron scattering	64

CONTENTS(cont.)

	Page
7.1.1 Proposal	65
7.1.1.1 Method and time estimate of the beamtime	65
7.1.1.2 List of relevant published literature and reference	66
7.1.2 reviews	67
REFERENCES	68
BIOGRAPHY	70

LIST OF TABLES

Table		Page
3.1	Summary of results for $\text{BaCu}_2\text{V}_2\text{O}_8$ from all papers	24
4.1	List of chemicals for sample preparation	27
4.2	XRD measurement parameters	30
4.3	Fitted parameters	31
5.1	Weight of prepared samples	43
5.2	Calculation of the susceptibilities in units of mol Cu	49
5.3	Fitted results for the isolated dimer model for $\text{BaCu}_2\text{V}_2\text{O}_8$ ($x = 0$)	51
5.4	Fitted results for the isolated dimer model for $\text{Ba}(\text{Cu}_{1-x}\text{Zn}_x)_2\text{V}_2\text{O}_8$ ($x=0.05$)	52
5.5	Fitted results for the isolated dimer model for $\text{Ba}(\text{Cu}_{1-x}\text{Zn}_x)_2\text{V}_2\text{O}_8$ ($x=0.1$)	53
6.1	Fitted parameters for magnetic susceptibility data of $\text{Ba}(\text{Cu}_{1-x}\text{Zn}_x)_2\text{V}_2\text{O}_8$	59

LIST OF FIGURES

Figure		Page
1.1	Super-exchange between spins	2
1.2	Phase diagram for the XXZ model	6
1.3	The singlet and triplet states in a spin $\frac{1}{2}$ chain	7
1.4	Chain of spin dimers with exchange interaction J	8
1.5	Magnetic susceptibility versus temperature T for the spin $S = 1/2$ antiferromagnetic (AF)	10
2.1	The XRD diffractometer	12
2.2	Beam path on the diffractometer	13
2.3	(a) The dc SQUID (b) current-voltage characteristics	16
2.4	MPMS system components	17
2.5	Scattering of neutron from a sample	19
3.1	Unit cell of $\text{BaCu}_2\text{V}_2\text{O}_8$	21
3.2	(a) The CuO_4 plaquettes (b) The exchange paths	21
3.3	The dominant spin exchange paths of $\text{BaCu}_2\text{V}_2\text{O}_8$	22
3.4	The thermal behaviour of $\text{BaCu}_2\text{V}_2\text{O}_8$	25
4.1	(a) The reagents used to prepare the sample, (b) scale (c) agate mortar	28
4.2	(a) Alumina (Al_2O_3) crucible, (b) platinum crucible, (c) Quartz crucible	29
4.3	Box furnace used to prepare the powder samples	29
4.4	Sample holder preparation	30
4.5	The lattice parameters c as a function of doping (x)	32
4.6	The lattice parameters a as a function of doping (x)	32
4.7	XRD diffraction profile of $\text{Ba}(\text{Cu}_{1-x}\text{Zn}_x)_2\text{V}_2\text{O}_8$ (a) $x=0$ and (b) $x=0.05$	33
4.8	XRD diffraction profile of $\text{Ba}(\text{Cu}_{1-x}\text{Zn}_x)_2\text{V}_2\text{O}_8$ (a) $x=0.1$ and (b) $x=0.15$	34

LIST OF FIGURES(cont.)

Figure	Page
4.9 XRD diffraction profile of $\text{Ba}(\text{Cu}_{1-x}\text{Zn}_x)_2\text{V}_2\text{O}_8$ (a) $x=0.2$ and (b) $x=0.3$	35
4.10 XRD diffraction profile of $\text{Ba}(\text{Cu}_{1-x}\text{Zn}_x)_2\text{V}_2\text{O}_8$ $x=0.4$	36
4.11 Effect of zinc doping on the spin chain	36
4.12 Bridgman-Stockbarger method	38
4.13 Furnace used for the Bridgman-Stockbarger method	40
4.14 Temperature profile of the furnace	41
4.15 Single crystal of $\text{BaCu}_2\text{V}_2\text{O}_8$ with dimension $\sim 1.5\text{mm}^3$	41
5.1 Capsule with powder sample	43
5.2 Measurement results for $\text{Ba}(\text{Cu}_{1-x}\text{Zn}_x)_2\text{V}_2\text{O}_8$ ($x = 0$)	44
5.3 Measurement results for $\text{Ba}(\text{Cu}_{1-x}\text{Zn}_x)_2\text{V}_2\text{O}_8$ ($x = 0.05$)	45
5.4 Measurement results for $\text{Ba}(\text{Cu}_{1-x}\text{Zn}_x)_2\text{V}_2\text{O}_8$ ($x = 0.1$)	45
5.5 Measurement results for $\text{Ba}(\text{Cu}_{1-x}\text{Zn}_x)_2\text{V}_2\text{O}_8$ ($x = 0.1$)	47
5.6 Measurement results for the background (teflon+capsule)	48
5.7 Temperature dependence of magnetic susceptibility of $\text{Ba}(\text{Cu}_{1-x}\text{Zn}_x)_2\text{V}_2\text{O}_8$	50
5.8 Temperature dependence of magnetic susceptibility of $\text{BaCu}_2\text{V}_2\text{O}_8$ with a fit (solid line) to the isolated dimer model	51
5.9 Temperature dependence of magnetic susceptibility of $\text{Ba}(\text{Cu}_{1-x}\text{Zn}_x)_2\text{V}_2\text{O}_8$ ($x=0.05$)	52
5.10 Temperature dependence of magnetic susceptibility of $\text{Ba}(\text{Cu}_{1-x}\text{Zn}_x)_2\text{V}_2\text{O}_8$ ($x=0.1$)	53
5.11 Temperature dependence of magnetic susceptibility of $\text{BaCu}_2\text{V}_2\text{O}_8$ after subtraction of the fitted Curie term	54
5.12 Matlab script for the simulation of the alternating chain model and the dimer model	55

LIST OF FIGURES(cont.)

Figure		Page
5.13	Fit of magnetic susceptibility of $\text{BaCu}_2\text{V}_2\text{O}_8$ to the alternating chain model with different value of alternation parameter α	56
5.14	Fit of magnetic susceptibility of $\text{BaCu}_2\text{V}_2\text{O}_8$ to the alternating chain model with $\alpha=1.97$ and $\Delta=468.9\text{K}$	56
6.1	Dependence of the spin gap (Δ/k_B) on doping (x) of $\text{Ba}(\text{Cu}_{1-x}\text{Zn}_x)_2\text{V}_2\text{O}_8$	60
6.2	Dependence of $N(\%)$ on doping (x) of $\text{Ba}(\text{Cu}_{1-x}\text{Zn}_x)_2\text{V}_2\text{O}_8$	60
6.3	Dependence of $N_{imp}(\%)$ on doping (x) of $\text{Ba}(\text{Cu}_{1-x}\text{Zn}_x)_2\text{V}_2\text{O}_8$	61
6.4	Alternating exchange model with zinc doping	62
6.5	Isolated dimer model with zinc doping	63
7.1	4SEASONS neutron spectrometer	64
7.2	Direct measurement of the spin gap in $\text{NaTiSi}_2\text{O}_6$	66

CHAPTER I

INTRODUCTION

1.1 Spin Exchange

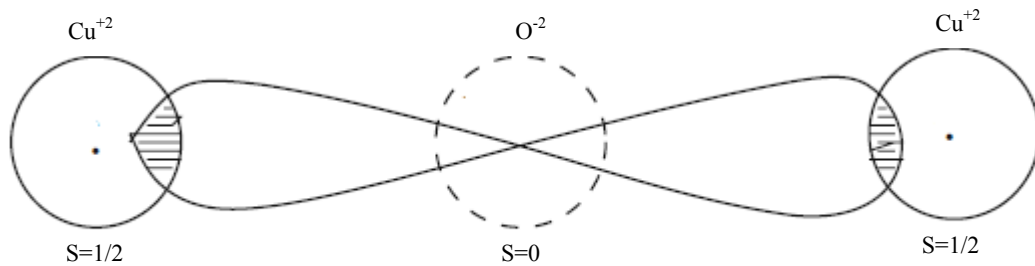
It was realized in the early days of quantum mechanics that the coupling mechanism between the magnetic moment in certain materials may lead to collective behaviours with macroscopic effects, such as ferromagnetism, where the moments line up parallel to each other, and antiferromagnetism, where neighbouring moments point in opposite directions. Classical dipolar interaction is too weak in order to explain the observed magnetic transition temperatures. This coupling is the so-called exchange interaction, introduced by Heisenberg and Dirac in the end of the 1920's [1, 2]. The exchange interaction has a quantum mechanical origin which derives from the fundamental properties of the electron: the electron spin, the electron kinetic energy, Pauli exclusion principle and the Coulomb repulsion between electrons. Interactions between two atoms with spins \mathbf{S}_1 and \mathbf{S}_2 would produce an effective interaction potential of the form:

$$V = J(\vec{R})\mathbf{S}_1 \cdot \mathbf{S}_2, \quad (1.1)$$

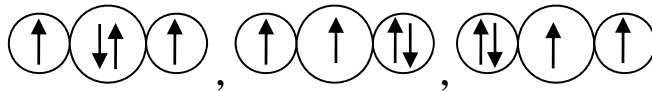
where $J(\vec{R})$ is the exchange energy, a function of the interatomic distance \vec{R} . The exchange energy is ferromagnetic if J is negative and antiferromagnetic if J is positive.

The exchange interaction can have different mechanisms, the two basic mechanisms are direct-exchange and indirect-exchange. In the direct-exchange, the ground state orbital wave functions of neighbouring atoms have a non-negligible overlap. The alignment of the spins is determined in order to minimize the interaction energy, depending on the nature of the non-interacting atomic states. The direct-exchange interaction falls off rapidly with distance, so that the interaction between further neighbours is effectively zero. In the indirect-exchange, the nearest neighbour spins are situated at a distance \vec{R} , which is large compared to the mean radius of the atomic ground state wave functions. There are a number of indirect exchange mechanisms, these include the RKKY interaction which is an example of indirect

exchange in metallic Heisenberg magnets, double-exchange and super-exchange which is relevant to magnetic insulators (localized magnetic moments). The exchange mechanism which is relevant for this work is the super-exchange so it will be explained with more detail. In super-exchange the actual exchange coupling results via non-magnetic ions (oxygen) that lie in between the magnetic ions (copper). The p-wavefunction of the anion overlaps with the d-wavefunctions of the cations so that electronic transitions are possible (hopping). The interactions between cations are mediated by the intermediate anions through a virtual double occupation of orbitals [Fig 1.1].



a. Ferromagnetic super-exchange states:



b. Antiferromagnetic super-exchange states:

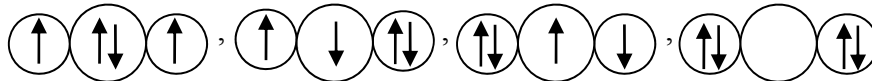


Figure 1.1 Super-exchange between spins (arrows) of Cu^{+2} cations (small circles) mediated by an O^{-2} anion (big circle).

1.2 One dimensional magnetism

The field of low-dimensional magnetism is one of the most active areas of today's solid state physics. Real magnetic materials are three-dimensional (3D) but can behave effectively as low-dimensional systems if the dominant exchange interactions between the magnetic moments (spins) are intra-chain (1D) or intra-planar (2D). The field of low-dimensional magnetism can be traced back to the origin of

quantum mechanics. In 1925 Ernst Ising studied the one-dimensional (1D) version of the model which is currently well known after his name in an effort to provide a microscopic justification for Weiss' molecular field theory of cooperative behaviour in magnets [3]. In 1931 Hans Bethe wrote his well-known paper [4] describing the 'Bethe ansatz' method, which can be used in order to find the exact quantum mechanical ground state of the antiferromagnetic Heisenberg model [5]. In the following years theorists succeeded in extending the solution of Ising's classical model to 2D, they have also succeeded in calculating correlation functions excitation energies, and thermal properties for the quantum mechanical 1D Heisenberg model as well as for some of its anisotropic generalizations. In another line of research theorists were able to establish the connection between quantum mechanical models in 1D and classical models in 2D. Around 1970 it became clear that the one and two dimensional models of interest may also be relevant for real materials which could be found in nature or be synthesized in a laboratory. These materials have made possible the verification and refinement of theoretical models for such systems. One-dimensional magnets provide the possibility to study ground and excited states of quantum models, possible new phases of matter and the interplay of thermal fluctuations and quantum fluctuations. Interest in the field increased with the discovery that high temperature superconductivity could probably be connected to the strong magnetic fluctuations which are possible in low dimensional materials. Examples of such one-dimensional materials include KCuF_3 and Sr_2CuO_3 which are among today's best realizations of the spin-1/2 antiferromagnetic Heisenberg model. Another widely investigated quasi-1D spin-1/2 antiferromagnet is CuGeO_3 , since in 1992 it was identified as the first inorganic spin-Peierls material [6] which is characterized by alternating deformation of the lattice along the chain direction, and singlet pair formations of the two $S=1/2$ spins on the shortened link. The theorem of Mermin and Wagner [7] states an important characteristic of low-dimensional magnets, which is the absence of long range order (LRO) in models that have a continuous symmetry at any finite temperature, and sometimes the absence of long range order in the ground state [8]. The Mermin Wagner theorem:

An infinite d dimensional lattice of localized spins cannot have LRO at any finite temperature for $d < 3$ if the effective exchange interactions among spins

are isotropic in spin space and of finite range.

When anisotropy is incorporated into the model (dipole-dipole interactions, non-isotropic exchange constants, single-ion anisotropy, etc.) it is again expected to find cases where low dimensional systems exhibit LRO.

Another interesting phenomena in one dimensional spin chains is fractional spin excitation where, in a magnetic-field, the phase of a spin-1/2 antiferromagnetic spin chain (see section 1.3) is fully polarized (spins parallel). In the fully polarized state the magnon can be represented as a firmly bound domain wall pair that propagates as a single entity. In this case the energy-momentum dispersion relation of the magnon will be discrete. In zero magnetic field, the spins are in the macroscopic singlet state $S_{\text{total}}=0$, an excitation of $\Delta S = 1$ above the singlet ground state (such as for a scattering of a neutron), may be imagined as a local spin flip surrounded by two domain walls. Due to the terms of the Hamiltonian that are transverse to the quantization axis the domain walls propagate individually and independently, in contrast to the fully polarized state where they propagate in pairs as a bound entity. The elementary excitation in zero-field ‘fractionalizes’ into two independent fermion-like objects known as ‘spinons’. The spinon carries spin-1/2 and can be associated with an individually propagating domain wall. Each spinon has a discrete energy-momentum relation and the excitation spectrum is composed of spinon pairs and will therefore be continuous. This characteristic continuous spectrum is observed at zero field, both experimentally (neutron scattering) and in exact calculations. An example of a system with fractional spinon excitations is $\text{CuSO}_4 \cdot 5\text{D}_2\text{O}$ [9].

1.3 Heisenberg model

The present work is restricted to the one-dimensional spin-1/2 Heisenberg model. A one-dimensional system (chain) composed of N localized and coupled spins-1/2 is described by the Heisenberg model:

$$\begin{aligned}
 H &= J \sum_{n=1}^N \hat{S}_n \hat{S}_{n+1} & (1.2) \\
 \hat{S}_n \hat{S}_{n+1} &= \hat{S}_n^z \hat{S}_{n+1}^z + \hat{S}_n^x \hat{S}_{n+1}^x + \hat{S}_n^y \hat{S}_{n+1}^y \\
 H &= \sum_{n=1}^N \left[J_{xy} \left(\hat{S}_n^x \hat{S}_{n+1}^x + \hat{S}_n^y \hat{S}_{n+1}^y \right) + J_z \hat{S}_n^z \hat{S}_{n+1}^z \right]
 \end{aligned}$$

The spin operators $\hat{S}_n^{\alpha,y,z}$ act only on the spin placed on site n. The couplings are limited to nearest-neighbour spins, J_{xy} is the strength of the flip-flop term $\left(\hat{S}_n^x \hat{S}_{n+1}^x + \hat{S}_n^y \hat{S}_{n+1}^y \right)$ which interchange up and down spins (for example $|\uparrow\downarrow\rangle$ to $|\downarrow\uparrow\rangle$), J_z is the strength of the Ising interaction $\hat{S}_n^z \hat{S}_{n+1}^z$. The ratio J_z / J_{xy} is the anisotropy, The model is isotropic when $J_z / J_{xy} = 1$, in which case it is known as the XXX model, and it is anisotropic when $J_z / J_{xy} \neq 1$, usually referred to as the XXZ model (XYZ also exists when the coupling strengths in the three directions are different). In a Hamiltonian containing only the Ising interaction, the ground state of the model depends on the sign of the interaction strength, it is ferromagnetic, with all spins aligned in the same direction, when $J_z < 0$, and it shows an antiferromagnetic arrangement with antiparallel neighbouring spins when $J_z > 0$.

1.3.1 XXZ model

The XXZ model can be written in the form:

$$H = J \sum_{n=1}^N \left[\left(\hat{S}_n^x \hat{S}_{n+1}^x + \hat{S}_n^y \hat{S}_{n+1}^y \right) + \Delta \hat{S}_n^z \hat{S}_{n+1}^z \right] + g \mu_B h \sum_n \hat{S}_n^z \quad (1.3)$$

Where an external field was added with an additional term in the Hamiltonian $g \mu_B h \sum_n \hat{S}_n^z$, where h is the external magnetic field chosen parallel to the z direction.

For $\Delta < -1$ the XXZ chain is in the ferromagnetic Ising phase: the ground state is the saturated state with all spins aligned in either z or $-z$ direction, For $\Delta > +1$ the XXZ chain is in the antiferromagnetic Ising or Neel phase The ground states have $S_{z,total} = 0$, but finite sublattice magnetization. For $-1 < \Delta < +1$ and zero external field the XXZ chain is in the XY phase.

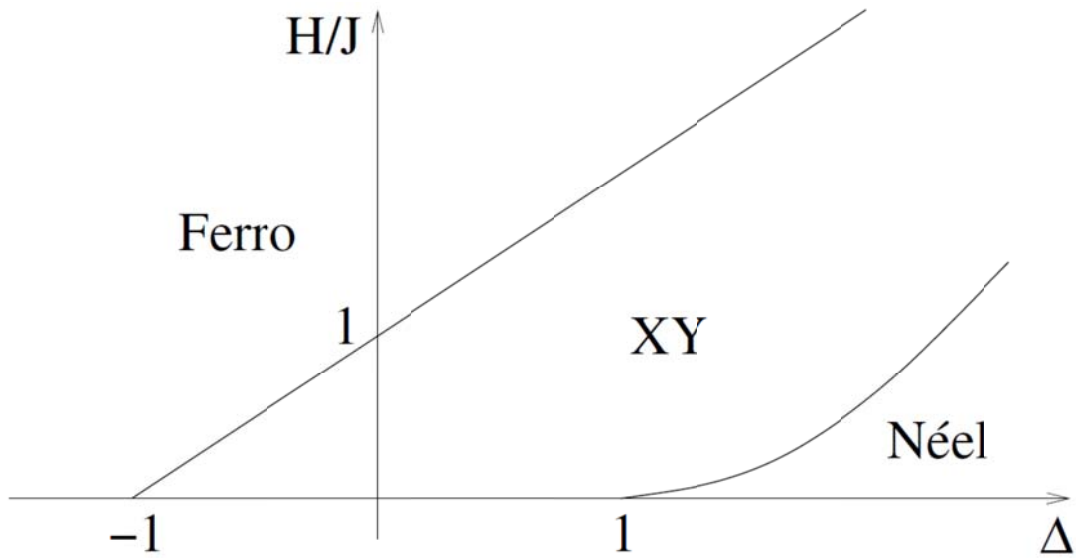


Figure 1.2 The boundary between the ferromagnetic phase and the XY phase is given by $H_c = \pm J(1 + \Delta)$. For $\Delta < 1$ (XY symmetry) the XY phase extends down to $H=0$. Figure from [10].

1.3.2 Alternating exchange in the $S = 1/2$ spin chain

Certain local constraints may prevent the system from reaching a local energy minimum, this causes frustration to arise in the system. In the case where the frustration arises due to the topology of the underlying lattice, the constraints are of geometric nature. If two terms in the Hamiltonian tend to favour incompatible configurations, then the constraints are of dynamical nature. A classical example of geometric constraints is that of an antiferromagnet in a triangular lattice with Ising interaction. This phenomenon can result in the appearance of ground state degeneracies. A prototype of a frustrated model in one dimension is the antiferromagnetic Heisenberg model with nearest and next-nearest neighbour interactions which is a modification to the ideal $S = 1/2$ XXZ chain.

The Hamiltonian is:

$$H = \sum_{n=1}^N J_1 \hat{S}_n \hat{S}_{n+1} + J_2 \hat{S}_n \hat{S}_{n+2} \quad (1.4)$$

$$H = J_1 \sum_{n=1}^N \hat{S}_n \hat{S}_{n+1} + \alpha \hat{S}_n \hat{S}_{n+2}$$

$$\alpha = \frac{J_2}{J_1}$$

Where α is the alternation parameter. The uniform AF Heisenberg chain is one limit of the alternating chain in which the two exchange constants are equal ($\alpha = 1, J_1 = J_2 \equiv J$). At the other limit is the isolated dimer in which one of the exchange constants is zero ($\alpha=0$).

1.3.3 Isolated dimer model

The case where $\alpha=0$ in the alternating exchange $S = 1/2$ spin chain, is known as the isolated dimer model. In this case, the strongly alternating exchange results in the formation of spin pairs, each pair is called a dimer [Fig 1.4]. Assuming that the coupling between dimers is small, one can neglect for each dimer all states except the two lowest ones, the singlet ($S=0$) and triplet ($S=1$) states. The Hilbert space is reduced to four states per dimer and two energy levels which are separated by an energy gap (Δ) [Fig 1.3].

State	S	S_z
$\frac{1}{\sqrt{2}} (\uparrow\downarrow\rangle - \downarrow\uparrow\rangle)$	0	0
$ \uparrow\uparrow\rangle$	1	1
$\frac{1}{\sqrt{2}} (\uparrow\downarrow\rangle + \downarrow\uparrow\rangle)$	1	0
$ \downarrow\downarrow\rangle$	1	-1

Figure 1.3 The singlet and triplet states in a spin $1/2$ chain, due to dimerization.

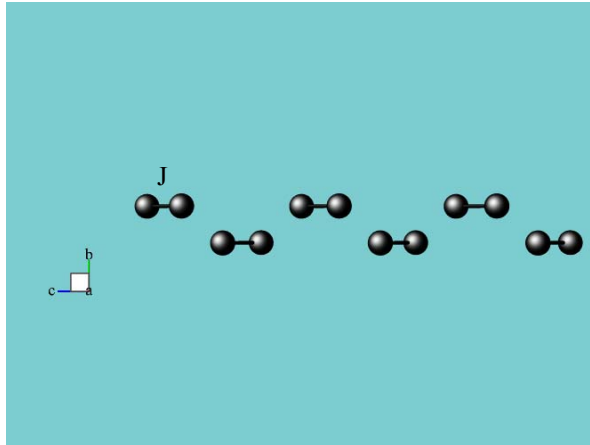


Figure 1.4 Chain of spin dimers with exchange interaction J .

1.4 Magnetization plateau

The phenomenon known as a magnetization plateau has been receiving much attention from both theoretically and experimentally. In low-dimensional spin systems with a spin gap, a sufficiently strong external magnetic field $H = H_c$ closes the gap, above H_c a finite magnetization will appear, in this high field phase the excitations may again acquire a gap, this makes the magnetization per spin m “locked” in some field range. The occurrence of a plateau and the physics of a high field critical phase in a strongly alternating $S=1/2$ zigzag chain, is explained in the following. The energy of the triplet state ($S_z=1$) becomes lower than the energy of the singlet state ($S_z=0$) at $H=J$. If the case where the dimers are completely decoupled, there would be just one critical field $H_c = J$ and at $H=H_c$ the magnetization M would jump from zero to one. The point $H=H_c$ will split into a small but finite field region $[H_c, H_s]$ in the presence of a finite weak interdimer coupling.

1.5 Thermodynamic properties of the Heisenberg $S = 1/2$ chain

The susceptibility and specific heat as function of temperature $\chi(T)$ and $C(T)$ are known exactly for the two limits of the alternating chain model. For the uniform chain ($\alpha=1$), $\chi(T)$ and $C(T)$ were estimated by Bonner and Fisher in 1964[11]. The exact solution for $\chi(T)$ of the uniform chain was obtained using the Bethe ansatz

in 1994 by Eggert, Affleck and Takahashi [12]. For the dimer ($\alpha=0$), Troyer, Tsunetsugu, and Wurtz[13] derived a general expression for $\chi(T)$. The exact solution at all temperatures is given by the equation:

$$\chi_{\text{spin-dimer}}(T) = Ng^2 \mu_B^2 / [k_B T (3 + e^{J/k_B T})], \quad (1.5)$$

where N is the number of spins which is twice the number of the formed dimer pairs in the chain. The two dimensional function $\chi(\alpha, T)$ was formulated by Johnston *et al*[14] using Quantum Monte Carlo (QMC) simulations and transfer-matrix density-matrix renormalization group (TMRG) calculations in the intermediate regime $0 < \alpha < 1$ and for the entire temperature range $T > 0.01 \cdot J_1/k_B$.

$$\chi_{\text{spin}}(\alpha, t) = \frac{Ng^2 \mu_B^2 e^{-\Delta_{fit}(\alpha)/t}}{J_{\text{max}} 4t} p_{m(8)}^{(7)}(\alpha, t) \quad (1.6)$$

$$p_{m(8)}^{(7)}(\alpha, t) = \frac{\left[\sum_{n=0}^6 N_n / t^n \right] + (N_{71}\alpha + N_{72}\alpha^2)(\Delta_0 / t)^y / t^7}{\left[\sum_{n=0}^7 D_n / t^n \right] + (D_{81}\alpha + D_{82}\alpha^2)(\Delta_0 / t)^z / t^8}$$

$$t = \frac{k_B T}{J_{\text{max}}}$$

$$N_n = \sum_{m=0}^4 N_{nm} \alpha^m$$

$$D_n = \sum_{m=0}^4 D_{nm} \alpha^m$$

$$\Delta_{fit}(\alpha) = 1 - \frac{1}{2}\alpha - 2\alpha^2 + \frac{3}{2}\alpha^3$$

$$\Delta_0(\alpha) = (1-\alpha)^{3/4} (1+\alpha)^{1/4} + g_1 \alpha (1-\alpha) + g_2 \alpha^2 (1-\alpha)^2$$

The constants N_{nm} , D_{nm} , y , z , g_1 , g_2 are numerically determined. A table with the calculated values of the parameters can be found in [14]. For the alternating chain systems, the spin gap for magnetic spin excitations from the $S=0$ singlet ground state to the lowest $S=1$ triplet excited states can be approximately expressed as follows:

$$\Delta = J_1 (1-\alpha)^{3/4} (1+\alpha)^{1/4}, \quad (1.7)$$

which is the analytic solution for $0 < \alpha < 0.9$.

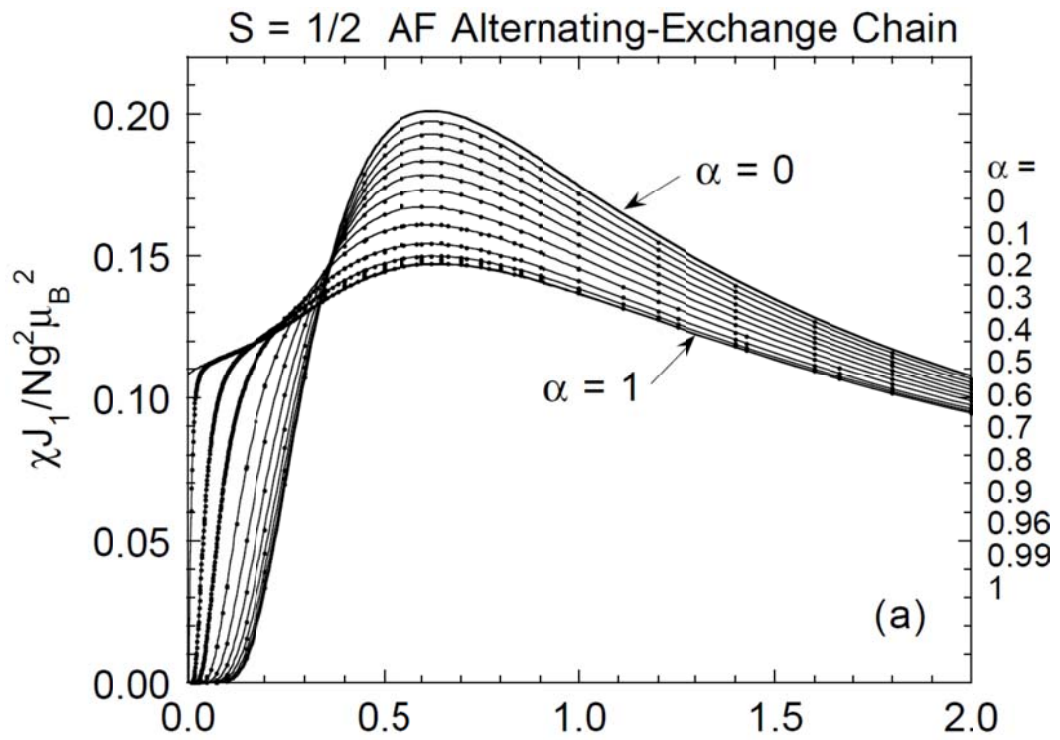


Figure 1.5 Magnetic susceptibility versus temperature T for the spin $S = 1/2$ antiferromagnetic (AF) alternating-exchange Heisenberg chain with alternation parameter $\alpha = J_2/J_1$ from 0 to 1. Figure taken from [14].

CHAPTER II

EXPERIMENTAL METHODS

2.1 Introduction

By comparing experimental results with theoretical predictions, it is possible to determine the microscopic spin Hamiltonian parameters (Such as J , Δ and α) in $\text{BaCu}_2\text{V}_2\text{O}_8$. This could help better understanding quantum magnetism in general. In this chapter the experimental methods which can be used in order to study the crystal structure (X-ray diffraction) and magnetic properties (SQUID, neutron scattering) of $\text{Ba}(\text{Cu}_{1-x}\text{Zn}_x)_2\text{V}_2\text{O}_8$, are described.

2.2 X-ray diffraction

A polycrystalline (powder) X-ray diffraction (XRD) experiment can be used for the determination of the crystal structure of materials. In an experiment the intensity of the beam, which is diffracted by a polycrystalline sample, is typically measured as a function of the Bragg angle (2θ), this is called the diffraction pattern. The presence of a crystalline phase is manifested in a diffraction pattern as a set of discrete intensity maximum, these are the Bragg reflections. Each intensity maximum has a specific location and intensity. When the atomic parameters, such as the coordinates of atoms in the unit cell and populations of different sites in the lattice of the crystalline phase are altered, this affects the relative intensities and/or positions of the Bragg peaks that correspond to this phase. A diffraction pattern consists of diffraction peaks (Bragg reflections) superimposed over a continuous background. Disregarding the background, the structure of a typical powder diffraction pattern may be described by the following components: positions, intensities, and shapes of multiple Bragg reflections. The three components contain information about the crystal structure of the material, the properties of the sample, and the instrumental parameters.

The peak positions can be used to determine the lattice parameters (a , b , c , α , β , γ), the peak intensity can determine the atomic parameters (coordinates of atoms in the unit cell and populations of different sites in the lattice). The peak shape can determine the crystallinity of the sample.

2.2.1 Instruments

In this work the measurements were made using Bruker D8 Advance powder diffractometer [Fig 2.1]. It has a Cu K radiation source (X-ray tube) which results in two peaks for each Bragg reflection $K_{\alpha 1}$ and $K_{\alpha 2}$ (K_{β} radiation is filtered). The radiation from the x-ray is diffracted at the sample and recorded by the detector. The sample rotates at constant angular velocity such that the angle of incidence of the beam changes whilst the detector rotates at a double angular velocity around the sample (Bragg–Brentano geometry [Fig 2.2]). The detector measures the intensity of the reflected radiation. Slits with different diaphragm width can be selected for the detector and aperture.

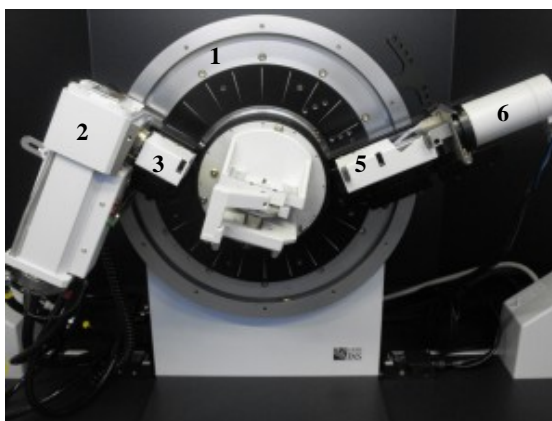


Figure 2.1 The diffractometer consists of the goniometer (1), the tube (2), the slit system (3, 5), the sample carrier (4), and the detector (6).

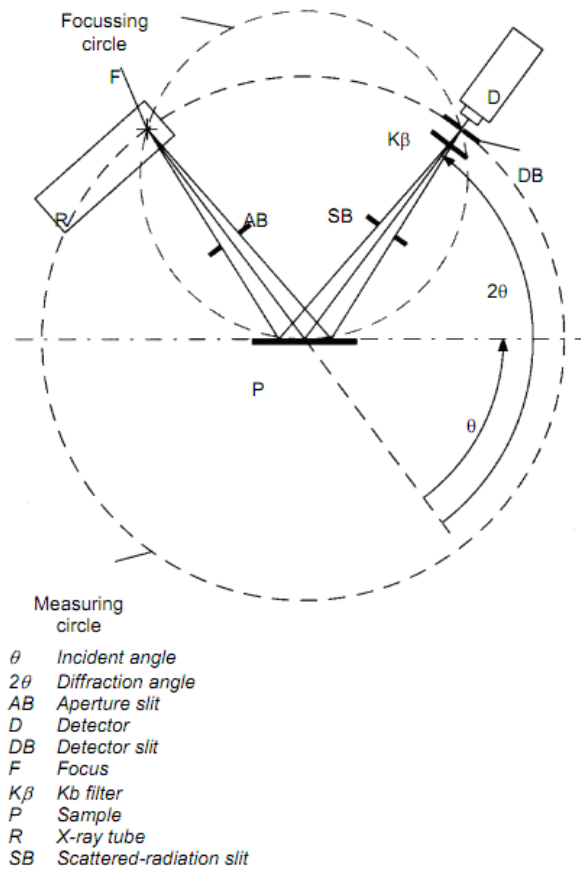


Figure 2.2 Beam path on the diffractometer.

2.2.2 Data analysis

After the measurement is made and the diffraction pattern is plotted, both the positions and intensities of the Bragg peaks need to be determined. Phase identification is accomplished by fitting the diffraction pattern of Bragg reflections with databases. Each diffraction pattern can be characterized by a unique distribution of the positions and intensities of Bragg peaks, the peak positions are determined by the unit cell dimensions and reflection intensities are determined by the distribution of atoms inside the unit cell. Each crystalline phase present in the sample will contribute to the pattern. The next step is to determine the lattice parameters precisely. When the goal of the experiment is only to identify phases which are present in the polycrystalline sample, it may be achieved in a fast experiment, An overnight experiment is required for indexing (assignment of hkl triplets) and accurate refinement of lattice parameters. Using known unit cell dimensions, indexing is usually

an easy task. It can be done by a computer program automatically. The low Bragg angle peaks are usually well-resolved and are located far apart from one another. Indices should always start from a peak observed at the lowest Bragg angle and proceed toward the higher Bragg angles. Using all Bragg peaks which have been indexed and the associated observed Bragg angles, more accurate unit cell dimensions can be refined by means of the Rietveld method. In the Rietveld method all structural and instrumental parameters are refined by fitting a calculated profile to the observed data. It is one of the fastest and perhaps the most reliable tool in quantifying phase contents. The main principle of this method is that the intensities calculated from the crystallographic data, are scaled to match the corresponding observed intensities in the same diffraction pattern via a common scale factor (k). In order to minimize the function Φ , given by:

$$Y_i^{calc} = kY_i^{obs} \quad (2.1)$$

$$\phi = \sum_i w_i (Y_i^{obs} - Y_i^{calc})^2$$

where w_i is the weight assigned to the i th data point, Y_i^{obs} is the observed and Y_i^{calc} is the calculated intensity of a point i of the powder diffraction pattern.

2.3 SQUID

The superconducting quantum interference device (SQUID) makes use of the physical phenomena of flux quantization as well as Josephson tunneling. The basis of the working principle of the dc SQUID is explained in the following. The dc SQUID consists of a superconducting ring, a Josephson junction is incorporated into each of the two arms. The ring is biased with a current I_b [Fig 2.3.a]. An external magnetic field $H = B/\mu_0$ is applied to the loop. The maximum supercurrent (I_c) that can flow across the ring is limited by the Josephson junctions to a maximum value which is given by the sum of the critical currents of the two junctions. The magnetic flux that flows through the SQUID ring causes I_c to modulate periodically, with a period that equals one flux quantum $\Phi_0 = h/2e$. The modulation is caused by an interference of the superconducting wave functions in the two arms of the SQUID. The voltage across the

junctions (V) can be read out directly as a function of the external magnetic field or applied magnetic flux if the SQUID is biased with a current slightly above the maximum value of I_c . In that case the voltage oscillates with a period which is equal to Φ_0 [Fig 2.3.b], counting the oscillations allows the evaluation of the flux change which has occurred. If a magnetized sample is moving through the ring the magnetic flux will be proportional to the speed and magnetization of the sample. To measure small changes in the applied flux $\Phi_a \ll \Phi_0$, the bias current can be chosen to maximize the amplitude of the voltage modulation and the applied flux is set at $(2n + 1)\Phi_0/4$ ($n = 0, 1, 2, \dots$), so that the flux-to-voltage transfer coefficient $|\partial V / \partial \Phi|$, which we denote as V_Φ is maximizes. In this way the SQUID will produce a maximum output voltage signal $\delta V = V_\Phi \delta \Phi$ in response to a small flux signal $\delta \Phi$ [Fig 2.3.c].

2.3.1 Instruments

In this work the measurements were performed at Tohoku University, Japan using Quantum Design Magnetic Property Measurement System (MPMS). This system integrates the following components [Fig 2.4]:

1. Temperature control module which regulates the thermal environment over the range of operation 1.9 to 400 Kelvin.
2. The superconducting magnet system which provides reversible field operation to plus and minus 5.5 Tesla.
3. The SQUID detector system
4. The sample handling system (translator and transport) which allows automatic position calibration with resolution .0003 cm.
5. Liquid helium system which provides refrigeration and gas handling system which provides gas flow control for temperature regulation.
6. The computer control system.

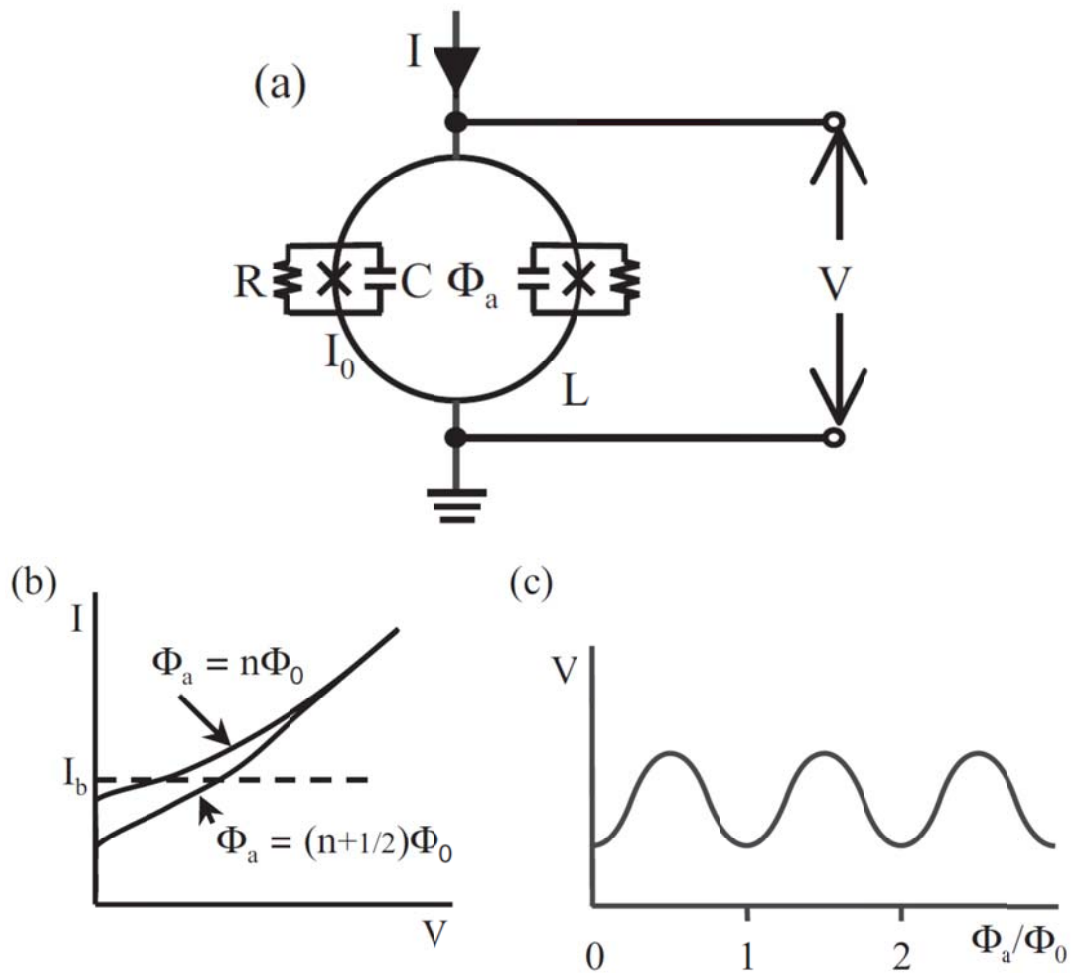


Figure 2.3 (a) The dc SQUID (b) current-voltage characteristics at integer and half-integer values of applied flux, the operation point is set by the bias current I_b (c) voltage vs flux Φ_a/Φ_0 for constant bias current. The periodic voltage response is due to the flux through the SQUID. The periodicity is equal to one flux quantum, Φ_0 .

MPMS SYSTEM COMPONENTS

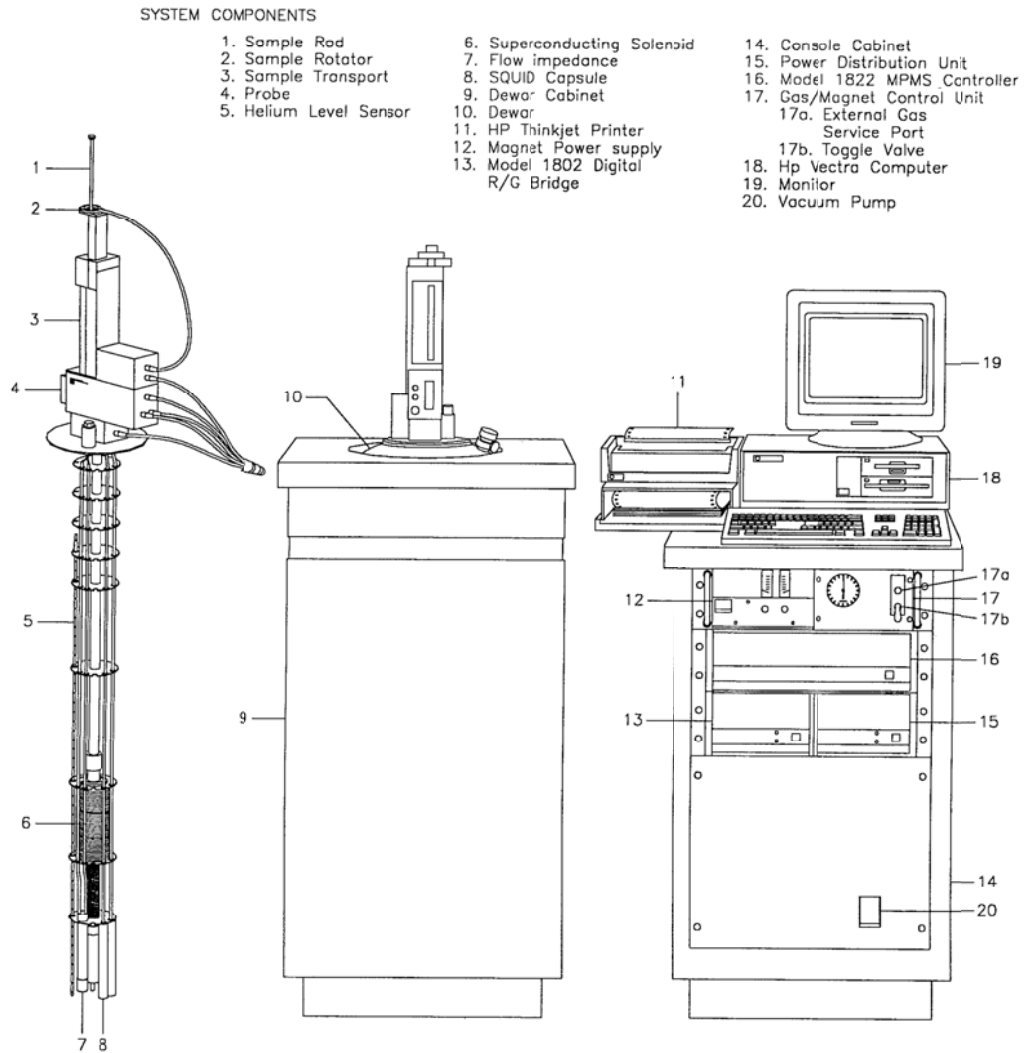


Figure 2.4 MPMS system components.

2.4 Neutron scattering

The advantages of using neutron scattering for material characterization come from the basic properties of the neutron:

1. Neutrons have no charge, they interact with the atomic nucleus and not with electrons. They are highly penetrating and produce very small disturbance in the sample.

2. The neutron carries magnetic moment which can be used as a probe for the magnetic properties of the material, such as magnetic ordering, magnetic excitations and spin fluctuations.

3. The magnetic scattering cross section and the nuclear scattering cross section have similar order of magnitude. Both nuclear and magnetic structure can be studied simultaneously.

In the experiment, the probability for a neutron which is incident on the sample with wave vector k_i to be scattered to wave vector k_f is measured [Fig 2.6]. From momentum and energy conservation:

$$\hbar Q = \hbar(k_i - k_f) \quad (2.2)$$

$$\hbar\omega = \frac{\hbar}{2m}(k_i^2 - k_f^2),$$

where $Q = k_i - k_f$. For elastic scattering $\hbar\omega = 0$, for inelastic scattering $\hbar\omega \neq 0$. The cross section formula for the neutron scattering experiment [Fig 2.5] is given by:

$$\frac{d^2\sigma}{d\Omega d\omega} = N \frac{k_f}{k_i} \left(\sum_{j,j'} b_j b_{j'} \right) \cdot S(Q, \omega) \quad (2.3)$$

where b_j is the scattering length of the nuclei, N is the number of atoms in the system and $S(Q, \omega)$ is the dynamical structure factor which corresponds to the probability for energy transfer $\hbar\omega$ and momentum $\hbar Q$ in the scattering of a neutron. The cross section corresponds to the number of neutrons scattered per second into a small solid angle $d\Omega$ [Fig 2.5] with energy transfer $\hbar\omega$ and $\hbar(\omega+d\omega)$, divided by the flux of incident neutrons. The cross section can be divided to two parts- coherent scattering in which neutrons scattered from different nuclei interfere and incoherent scattering in which there is no interference and the intensities from each nuclei add up independently. Elastic coherent scattering can be used to study the equilibrium structure and inelastic coherent scattering can be used to study collective motion of atoms (phonons).

Incoherent elastic scattering is the same in all directions, so it usually appears as unwanted background in neutron scattering experiments. Incoherent inelastic scattering provides information about atomic diffusion. The dipole-dipole interaction between the neutron and nuclei gives rise to a magnetic cross section, the result of neutron scattering experiment is a diffraction pattern with both nuclear and magnetic peaks which enables the solution of the material nuclear and magnetic structure.

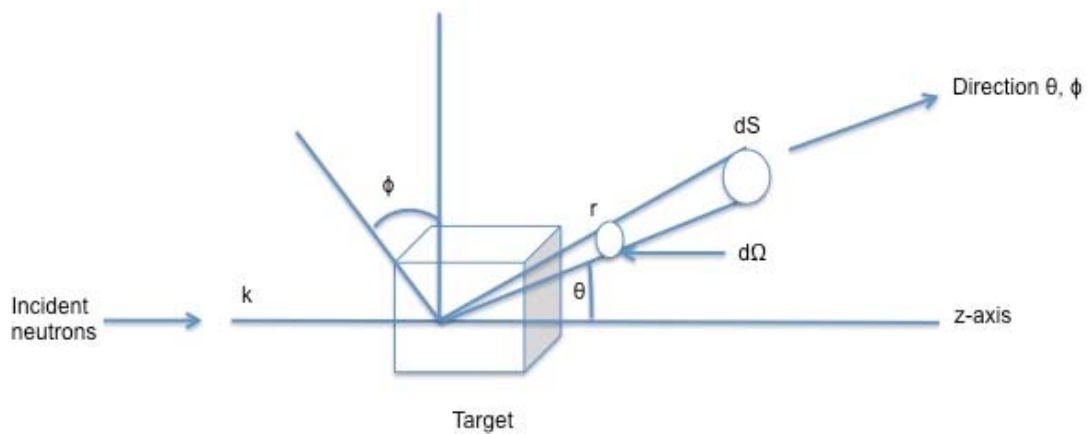


Figure 2.5 Scattering of neutron from a sample.

CHAPTER III

LITERATURE REVIEW

3.1 Crystal structure of $\text{BaCu}_2\text{V}_2\text{O}_8$

$\text{BaCu}_2\text{V}_2\text{O}_8$ compound was first synthesized by R. Vogt *et al.* in 1990 [15] and its crystal structure was reported to have tetragonal symmetry of space group I-42d (#122) with $a=b=12.744\text{\AA}$, $c=8.148\text{\AA}$ and $Z=8$ [Fig 3.1]. The Cu^{2+} ($S=1/2$) ions are bridged by oxygen ions, forming CuO_4 square plaquettes. V^{5+} ions ($S=0$) have two non-equivalent crystallographic sites which are coordinated inside oxygen tetrahedral. One-dimensional linear chains are made of the edge-sharing pairs of CuO_4 square-plaquettes and the VO_4 tetrahedral (V(1) site) along the c axis, the linear chains are separated by another VO_4 tetrahedral (V(2) site) [Fig 3.2].

3.2 Theoretical Model

$\text{BaCu}_2\text{V}_2\text{O}_8$ is one of the promising candidates for spin-1/2 one-dimensional Heisenberg antiferromagnetic (HAF) chain systems with a spin gap. A spin gap (Δ) can open up in HAF spin chains due to the difference between the nearest-neighbour and next-nearest-neighbour exchange interactions, which in some case causes the dimerization of a spin pair called a dimer. The spin-1/2 alternating-exchange HAF chain Hamiltonian is written as $H=J_1\sum_i(S_{2i-1}\cdot S_{2i}+\alpha S_{2i}\cdot S_{2i+1})$ where the alternation parameter $\alpha\equiv J_2/J_1$. The limit in which the exchange constants is zero ($\alpha=0$) is called the isolated dimer.

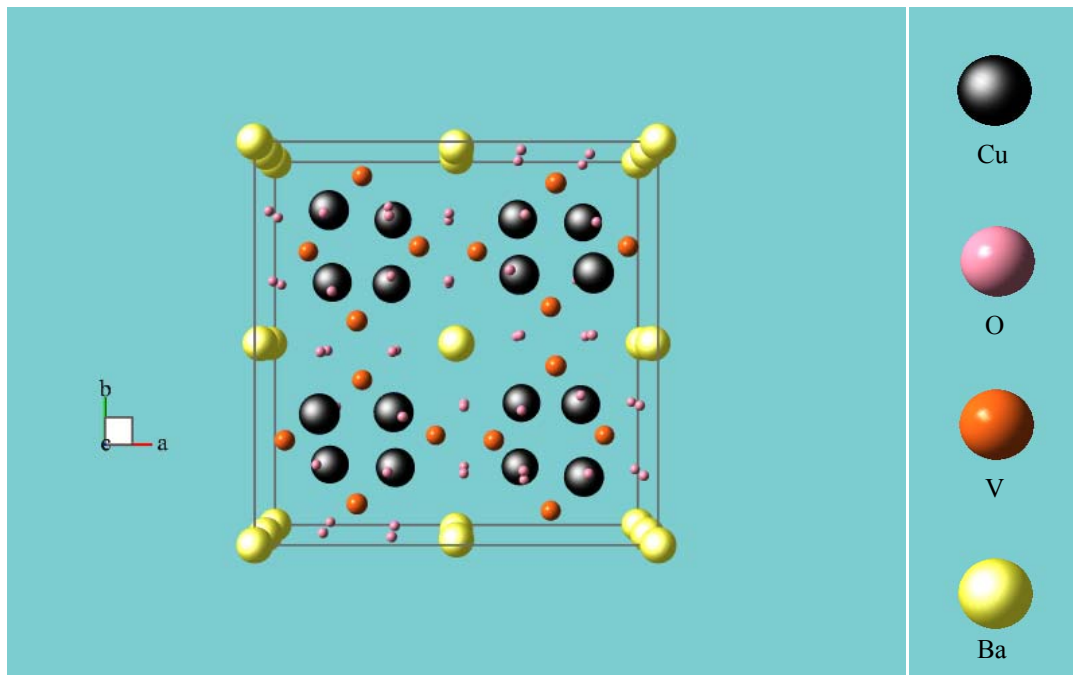


Figure 3.1 Unit cell of $\text{BaCu}_2\text{V}_2\text{O}_8$ Tetragonal symmetry, space group $I-42d$ Lattice constants: $a=b=12.744\text{\AA}$; $c=8.148\text{\AA}$

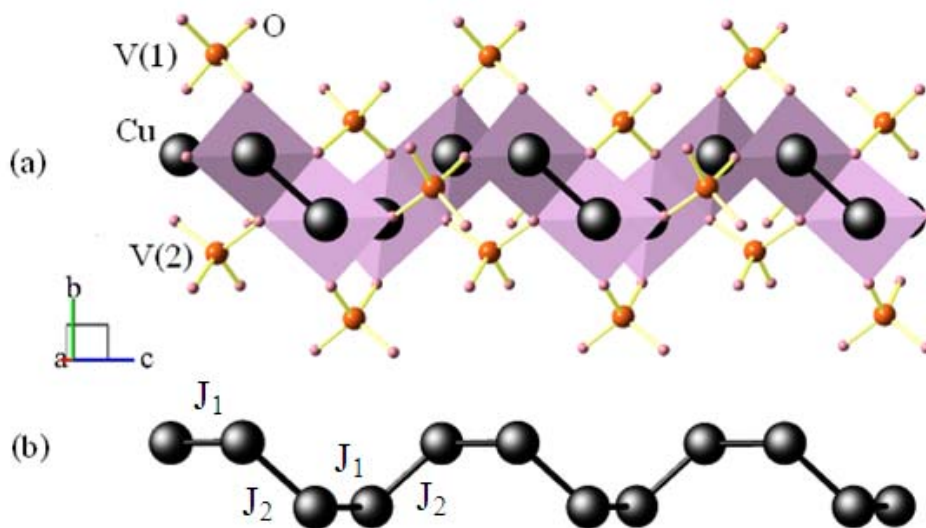


Figure 3.2 (a) The CuO_4 plaquettes form two parallel chains along the c direction bridged by $\text{V}(1)$, $\text{V}(2)$, and oxygens. (b) The exchange paths J_1 and J_2 alternate along the chain.

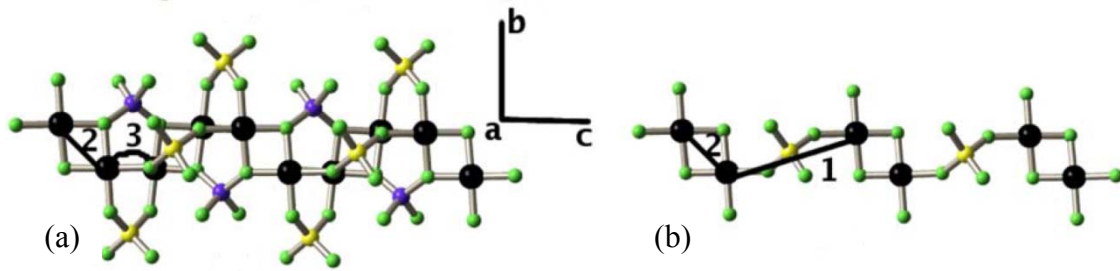


Figure 3.3 The dominant spin exchange paths of $\text{BaCu}_2\text{V}_2\text{O}_8$ as proposed by Koo and Whangbo [19] (a) and He *et al.* [18] (b). Figure taken from [20].

3.3 Experimental results

He *et al.* [16][17] suggested that a large spin gap Δ is favourable for the increment of doping concentrations, due to the fact that the depression of the spin gap which accompanies the appearance of various AF phases, has a linear relation with the increment of impurity doping. This may attract scientific interest for the investigation of new magnetic phenomena. In their search for compounds with a large spin gap, they have studied $\text{BaCu}_2\text{V}_2\text{O}_8$ by means of magnetic susceptibility and heat capacity measurements on a powder and single crystal samples and reported a large spin gap of $\Delta = 230\text{K}$, they identified the dominant exchange paths and claimed that the magnetic susceptibility was well reproduced by a strongly alternating AF chain model with $J_1 = 260\text{K}$ for the Cu-O-V-O-Cu path, $J_2 = 52\text{K}$ for the Cu-O-Cu path and $\alpha = 0.2$ [Fig 3.3.b]. However later reports show inconsistencies in the dominant exchange paths and alternation parameter α . ^{51}V NMR study by Lue and Xie [18] examined both alternating-chain and dimer-chain models and suggested that both scenarios are suitable for the understanding of the spin gap nature in $\text{BaCu}_2\text{V}_2\text{O}_8$, for the alternating-chain model they calculated $\alpha = 0.1$ and $\Delta = 370\text{K}$ and for the dimer-chain model they calculated $\Delta = 450\text{K}$. Koo and Whangbo [19] based on extended Hückel tight-binding calculations, determined the dominant exchange path and found an alternation parameter close to $\alpha = 0.1$. The dominant exchange paths are different from those suggested by He *et al.* [Fig 3.3.a].

The latest publication about this subject from Sarita *et al.* [20] points to problems with the data analysis of the susceptibility measurement by He *et al.* They

repeated the measurement and showed that the data is best fitted with the isolated dimer model using the general expression for $\chi(T)$ derived by Johnston *et al.* [14], which gives the exact solution of the magnetic susceptibility for all temperatures in the case of the one-dimensional (1D) $S = 1/2$ isolated dimer Heisenberg spin systems with a spin gap. Sarita *et al.* [20] obtained a gap $\Delta = 470$ K with $\alpha = 0$ which compares closely with the gap value of $\Delta = 450$ K obtained by Lue and Xie by their nuclear magnetic resonance (NMR) investigation using the isolated dimer model. In addition they calculated the dominant exchange path by calculating the effective Cu-Cu hopping integrals using the self-consistent tight-binding linearized muffin-tin orbital (LMTO) method. They found that the dominant hopping parameter is the one mediated by the O-V-O complex [Fig 3.3.a label 3]. The next dominant interaction is the interaction between the two Cu ions in a Cu_2O_6 plaquette [Fig 3.3.a label 2] and the other hoppings are negligible resulting in the alternation parameter $\alpha = J_3/J_2 = 0.05$ which is close to zero and supports the isolated dimer model. Their calculations provides justification for the chain topology suggested by Koo and Whangbo [19] [Fig 3.3.a] but a smaller value for α . ^{51}V NMR studies by K. Ghoshray *et al* [21] in polycrystalline sample reveal the existence of nonzero spin densities, with unequal magnitudes, at the two vanadium sites, V_1 and V_2 and hence the participation of VO_4 tetrahedral in the intrachain and interchain exchange interaction. The data also shows clear signature of the reduction of Cu^{2+} spin susceptibility within the chain and indicate a comparatively weaker exchange path in between the chains. The shift data further confirms that there exists a nonmagnetic ground state. The spin gap from the shift data of V_1 and V_2 is valued $\Delta = 215\text{K}$, from the spin-lattice relaxation times $\Delta = 380\text{K}$, and from susceptibility $\Delta = 230\text{K}$. C. S. Lue *et al* [22] measurements of the thermal conductivity (κ) with heat flow parallel and perpendicular to the chain axis. A weak but non-negligible contribution to κ along the chain has been identified, attributed to the magnon heat transport. Hyun-Joo Koo [23] studied the importance of the O- V^{5+} -O bridges and determined that the VO_4 tetrahedral, are crucial for the spin-exchange interactions and hence for deducing the spin-lattice models needed to interpret the magnetic properties. The different results from different groups are summarized in Table 3.1.

Table 3.1 Summary of results for BaCu₂V₂O₈ from previous works.

	Method	Results
He <i>et al</i> (2004-2006) [16,17]	Magnetic susceptibility, Heat capacity	$\Delta = 230\text{K}$ $\alpha = 0.2$ (alternating-chain) Exchange paths (b)
Lue and Xie (2005) [18]	NMR	Both alternating-chain and dimer are suitable: $\alpha = 0.1$, $\Delta = 370\text{K}$ Dimer, $\Delta = 450\text{K}$
Ghoshray <i>et al</i> [21]	NMR, Magnetic susceptibility	Alternating-chain Shift data: $\Delta = 215\text{K}$ Relaxation times: $\Delta = 380\text{K}$ Susceptibility: $\Delta = 230\text{K}$.
Koo and Whangbo (2006) [19]	Electronic structure calculations	Exchange paths (a) $\alpha = 0.1$
Sarita <i>et al</i> (2008) [20]	Magnetic susceptibility, Electronic structure calculations	Dimer $\Delta = 470\text{K}$ Exchange paths (a)

3.3.1 Zinc doped BaCu_{2-x}Zn_xV₂O₈

A study of the zinc doped Ba(Cu_{1-x}Zn_x)₂V₂O₈ was made by means of magnetic susceptibility measurements by H. Sakurai [24] and NMR by Lue and Xie [25]. Both studies show that the spin gap is insensitive to the doping level. These results suggest that the dimer pair is almost isolated ($\alpha=0$). However, there are problems with the data analysis by H.Sakurai. The $\chi(T)$ model for a 1D alternating chain, which is correctly described by $\chi = AT^{-1/2}\exp(-\Delta/T) + C/(T-\Theta) + \chi_0$, where χ_0 is a temperature-independent term, C the Curie constant, Θ the Weiss temperature, and Δ the spin gap, is only valid for low- T ($T < 120\text{K}$). In their analysis the susceptibility measurements for $T < 120\text{K}$ were fitted to a wrong model with the first term replaced with $A\exp(-\Delta/T)$. The resulting spin gap they calculated was $\Delta/k_B = 343\text{K}$ for the

undoped sample. This result is in contrast to the spin gap $\Delta/k_B = 230\text{K}$ calculated using the correct model for the same measurement by He et al [16, 17]. In addition, later studies show that the isolated dimer model, instead of the alternating chain model, is better suited for this system [20]. In the NMR study by Lue and Xie, the doped samples were prepared up to $x=0.25$; however they do not mention any XRD measurements in order to verify that the doped samples still match the $\text{BaCu}_2\text{V}_2\text{O}_8$ phase.

3.4 Crystal growth

He *et al.* [26] grew High-quality large single crystals of $\text{BaCu}_2\text{V}_2\text{O}_8$ with dimensions $25 \times 10 \text{mm}$ by top-seeded growth method using V_2O_5 as self-flux. They found that using 5% self flux and a temperature gradient of $5\text{C}^\circ/\text{cm}$ is favourable for crystal growth. The thermal behaviour of $\text{BaCu}_2\text{V}_2\text{O}_8$ has been investigated using differential thermal analysis (DTA) [Fig 3.4]. There are three peaks in the plot, it is suggested that the former is linked with the phase transition, the middle the melting point, and the latter the decomposition of the melt as seen in loss in weight of TG curve. This shows that $\text{BaCu}_2\text{V}_2\text{O}_8$ is decomposed at a temperature close to its melting point which makes the flux method (lowering the melting point) suitable for its crystal growth. They also mentioned that further studies on spin dynamics using the grown crystal are in progress, however they still have not published on this topic.

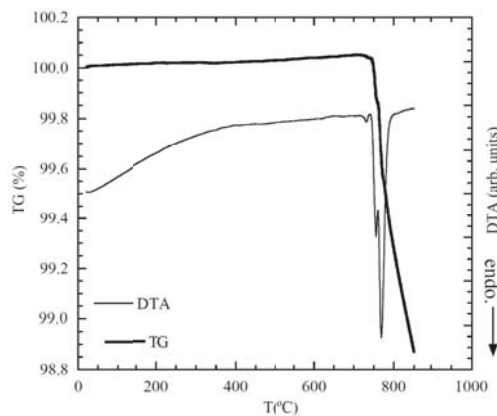


Figure 3.4 The thermal behaviour of $\text{BaCu}_2\text{V}_2\text{O}_8$. Peaks in DTA ($730, 760, 770\text{ }^\circ\text{C}$). Figure taken from [26]

3.5 Motivation

$\text{BaCu}_2\text{V}_2\text{O}_8$ is one of the promising candidates for spin-1/2 one-dimensional Heisenberg antiferromagnetic (HAF) chain systems with a spin gap. Such one-dimensional systems can exhibit a variety of novel phenomena related to spin and charge correlation [27], such as the spin-Peierls state, the Bose-Einstein condensation of magnons, and the fractional spinon excitations in a quantum spin liquid state. It is important to study the spin dynamics and determine the microscopic spin Hamiltonian parameters in these systems in order to compare experimental results with theoretical predictions and for better understanding quantum magnetism in general. A spin gap (Δ) can open up in HAF spin chains due to the difference between the nearest-neighbour and next-nearest-neighbour exchange interactions, which in some cases causes the dimerization of a spin pair called a dimer. The origin of the spin gap in $\text{BaCu}_2\text{V}_2\text{O}_8$ is still not completely determined, as can be seen from the results that were reported by different groups [Table 3.1]. There is a difficulty determining the most suitable model for this system, using only the previously mentioned experimental methods. Fitting the experimental results with theoretical models gives different results that can imply that both the isolated dimer model and alternating exchange model with $\alpha=0.1$ and $\alpha=0.2$ can be used.

In order to be able to better determine the most suitable model for this system, zinc doping of the compound can be used to introduce spin vacancies into the chain and study their effect on the exchange interactions. Previous studies on zinc doped $\text{BaCu}_2\text{V}_2\text{O}_8$ have some problems in their data analysis and are also outdated in view of the more recent studies on the undoped $\text{BaCu}_2\text{V}_2\text{O}_8$.

Due to the inconsistency and problems with all previous publications, the study of both undoped $\text{BaCu}_2\text{V}_2\text{O}_8$ and the zinc doped $\text{Ba}(\text{Cu}_{1-x}\text{Zn}_x)_2\text{V}_2\text{O}_8$ was repeated in this work using susceptibility measurements, while performing the correct analysis.

Another method that can be used in order to determine the most suitable model is a direct measurement of the spin gap (Δ) using inelastic neutron scattering. This measurement is made preferably on a sufficiently large single crystal sample. This method will also be discussed in this work.

CHAPTER IV

SAMPLE PREPARATION AND CHARACTERIZATION

4.1 Polycrystalline $\text{BaCu}_2\text{V}_2\text{O}_8$

Polycrystalline $\text{Ba}(\text{Cu}_{1-x}\text{Zn}_x)_2\text{V}_2\text{O}_8$ ($x = 0, 0.05, 0.1, 0.15, 0.2, 0.3$ and 0.4) were synthesized by a standard solid-state reaction method using high-purity reagents (in order to increase the purity of the synthesized samples) of BaCO_3 , CuO , ZnO and V_2O_5 in the stoichiometric ratio. The chemical equation is:

$\text{BaCO}_3 + 2((1-x)\text{CuO} + (x)\text{ZnO}) + \text{V}_2\text{O}_5 = \text{Ba}(\text{Cu}_{1-x}\text{Zn}_x)_2\text{V}_2\text{O}_8 + \text{CO}_2$, where $x = 0, 0.05, 0.1, 0.15, 0.2, 0.3$ and 0.4 . The amount of zinc doping (x) was chosen in order to be able to collect data over a wide range ($x=0$ to $x=0.4$) while not changing the structure of the spin chain. Substituting copper ions (spin $1/2$) with zinc ions (spin zero) in the same chain structure allows the study of the effect of spin vacancies on the exchange interaction.

Table 4.1 List of chemicals for sample preparation

Chemical	Formula	Purity	Company
Barium carbonate	BaCO_3	>99%	Sigma-Aldrich
Copper oxide	CuO	>99%	Aldrich
Zinc oxide	ZnO	>99%	Sigma-Aldrich
Vanadium oxide	V_2O_5	>98%	Aldrich

The reagents were carefully weighed and mixed with ethanol, then carefully ground, and thoroughly homogenized in an agate mortar until the ethanol was dried [Fig 4.1]. The mixture was heated inside an alumina (Al_2O_3) crucible [Fig 4.2.a] at 500°C for 24h in air using the box furnace [Fig 4.3] then cooled to room temperature and ground again. The mixture was then packed into a quartz crucible [Fig 4.2.c] and heated at 750°C for 60h with two intermediate grindings. There was no chemical reaction between the alumina and quartz crucibles and the polycrystalline

compound. Intermediate grindings were used in order to increase surface area and assist with the chemical reaction process. In the case of an incomplete reaction (which can be determined by XRD), the sample was placed in the furnace for an additional heating cycle for 24h at 750⁰C

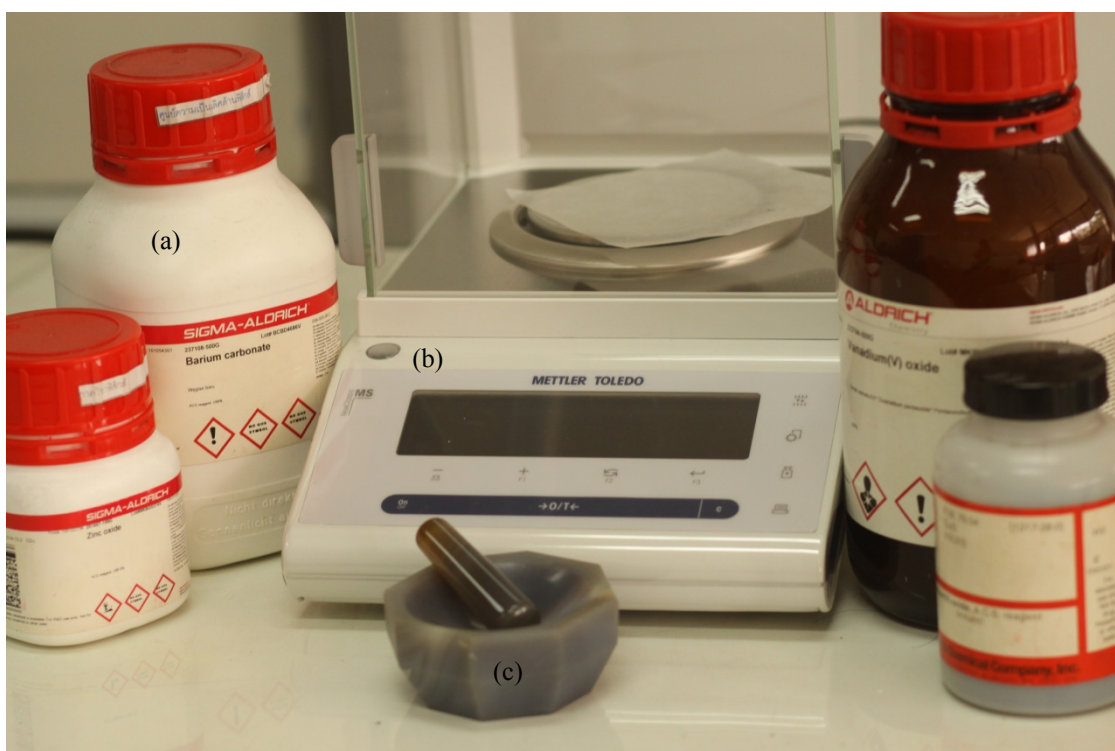


Figure 4.1 (a) The reagents used to prepare the sample, (b) scale, (c) agate mortar.

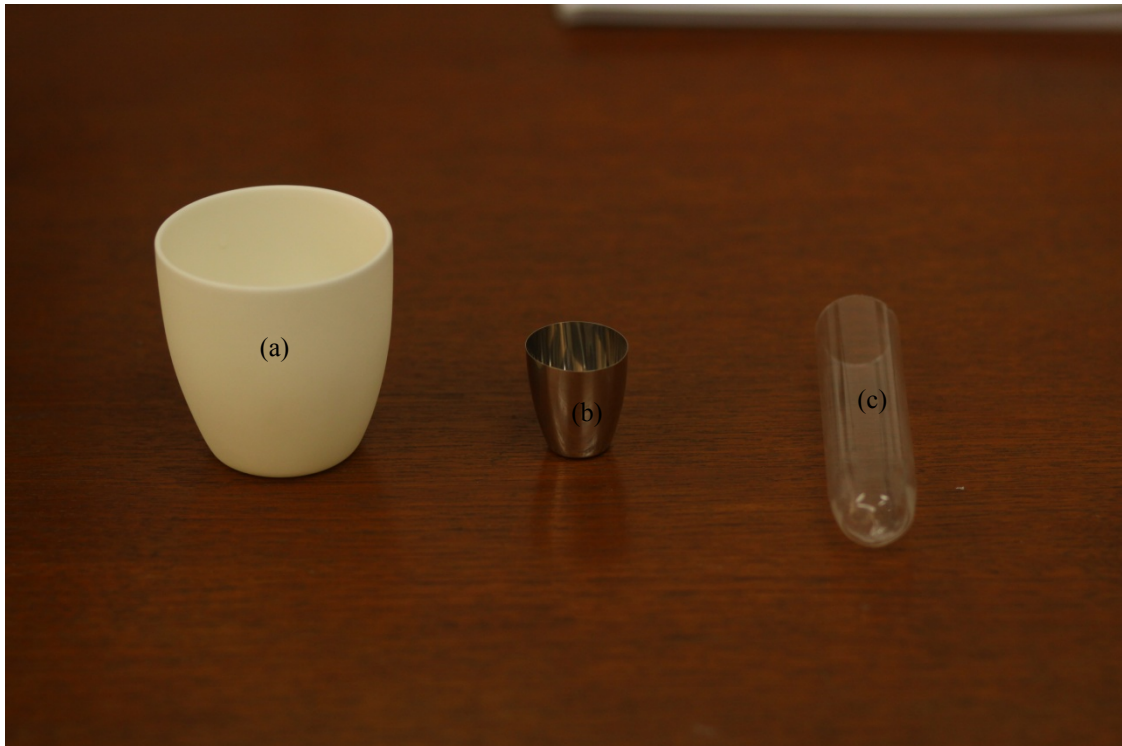


Figure 4.2 (a) Alumina (Al_2O_3) crucible, (b) platinum crucible, (c) Quartz crucible.



Figure 4.3 Box furnace used to prepare the polycrystalline samples.

4.2 Sample characterization

XRD measurements and data processing were made using the instrument describes in chapter II. Slits with diaphragm width of 1mm were selected for the detector and aperture. Each sample was placed in a sample holder of diameter 1.4cm. This gives a large enough sample surface area for the x-ray beam with the selected diaphragm width, at all scattering angles. The method described in Figure 4.4 was used in order to avoid preferred orientation of the particles (which could affect the resulting intensities in the diffraction pattern). The scan was made using the parameters in Table 4.2. Longer step time and larger scattering angle range were chosen for the undoped sample. This is because for the undoped sample, the date was used in order to get the best fit to the structure file and confirm the phase. For the undoped samples the data was used in order to make sure there are no impurities (complete chemical reaction) and also in order to fit the lattice parameters, this does not require long measurements.

Table 4.2 XRD measurement parameters

Parameter	Undoped sample ($x=0$)	Doped samples ($x=0,05,0.1,0.15,0.2,0.3,0.4$)
2θ	5-80 ⁰	18.5-64 ⁰
Step size	0.02 ⁰	0.02 ⁰
Time/step	10seconds	5seconds

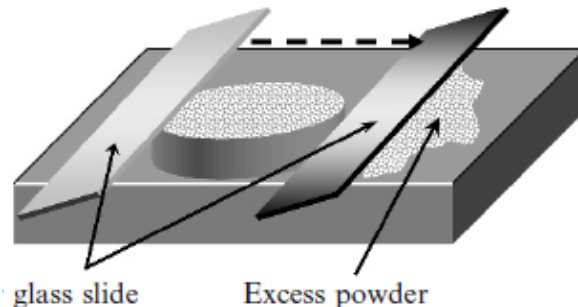


Figure 4.4 The powder sample is placed in the sample holder without packing (pressing against a smooth surface). Excess powder is removed from the top of the sample holder with a single sweep by a glass slide. This ensures that the particles in the sample holder are randomly oriented as required.

The measured diffraction patterns of the undoped and doped samples were fitted to the $\text{BaCu}_2\text{V}_2\text{O}_8$ structure file (.cif) from the Crystallography Open Database [25] by means of Rietveld refinement (see chapter II) using FullProf [Fig 4.7, 8, 9, 10]. The results of the fits are given in Table 4.3. For the fitting procedure, the fitting parameters were refined in the following steps for each measurement (each parameter is added to the previous parameters):

1. Scale, peak shape function.
2. Three background coefficients
3. Zero (Sample position)
4. Lattice constants
5. U parameter
6. Atom positions
7. Preferred orientation with $hkl=420$

Using this step process resulted in the lowest values for χ^2 . Samples with doping percentage up to 40% showed no impurity and gave a good fit to the structure file as can be seen from the low values of χ^2 [Table 4.3] which means that zinc was successfully substituted for copper [Fig 4.10]. The lattice parameters for each sample were estimated from the peak positions in the diffraction pattern. The results show that the lattice parameter a linearly decreases and c linearly increases with higher doping (x) [Fig 4.5, 6].

Table 4.3 fitted parameters.

	χ^2	$a(\text{\AA})$	$a(\text{\AA})$ standard deviation	$c(\text{\AA})$	$c(\text{\AA})$ standard deviation
x=0	1.4	12.76604	$2.3 \cdot 10^{-4}$	8.15093	$1.8 \cdot 10^{-4}$
x=0.05	1.63	12.75398	$2.9 \cdot 10^{-4}$	8.16181	$2.3 \cdot 10^{-4}$
x=0.1	1.58	12.74265	$3.3 \cdot 10^{-4}$	8.17575	$2.5 \cdot 10^{-4}$
x=0.15	1.69	12.72991	$4.0 \cdot 10^{-4}$	8.18751	$3.0 \cdot 10^{-4}$
x=0.2	2.36	12.71911	$15.5 \cdot 10^{-4}$	8.20139	$10.8 \cdot 10^{-4}$
x=0.3	1.59	12.68227	$4.7 \cdot 10^{-4}$	8.22240	$3.5 \cdot 10^{-4}$
x=0.4	1.69	12.65096	$4.5 \cdot 10^{-4}$	8.25001	$3.5 \cdot 10^{-4}$

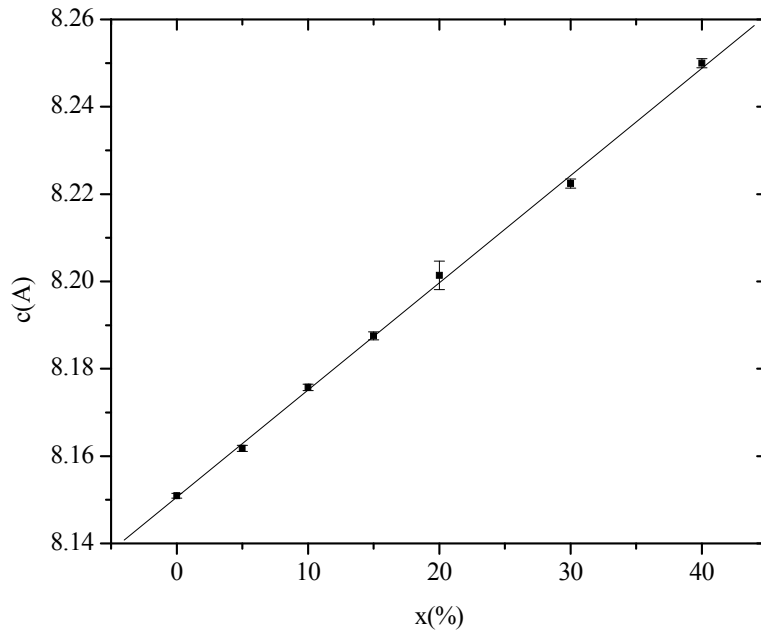


Figure 4.5 The lattice parameters c as a function of doping (x). Data with error bars (standard deviation $\times 3$) and linear fits (solid line). $c = 8.15056 + 0.00246x$.

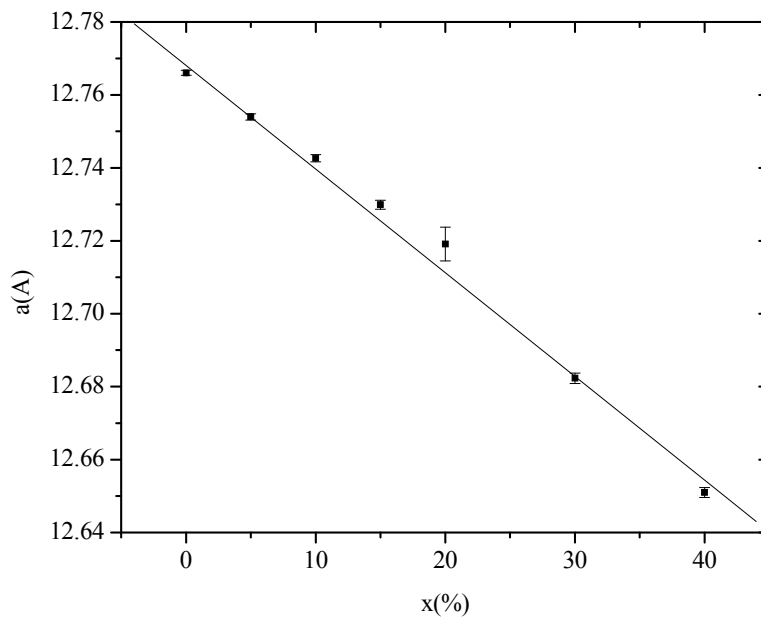


Figure 4.6 The lattice parameters a as a function of doping (x). Data with error bars (standard deviation $\times 3$) and linear fits (solid line). $a = 12.76811 - 0.00284x$.

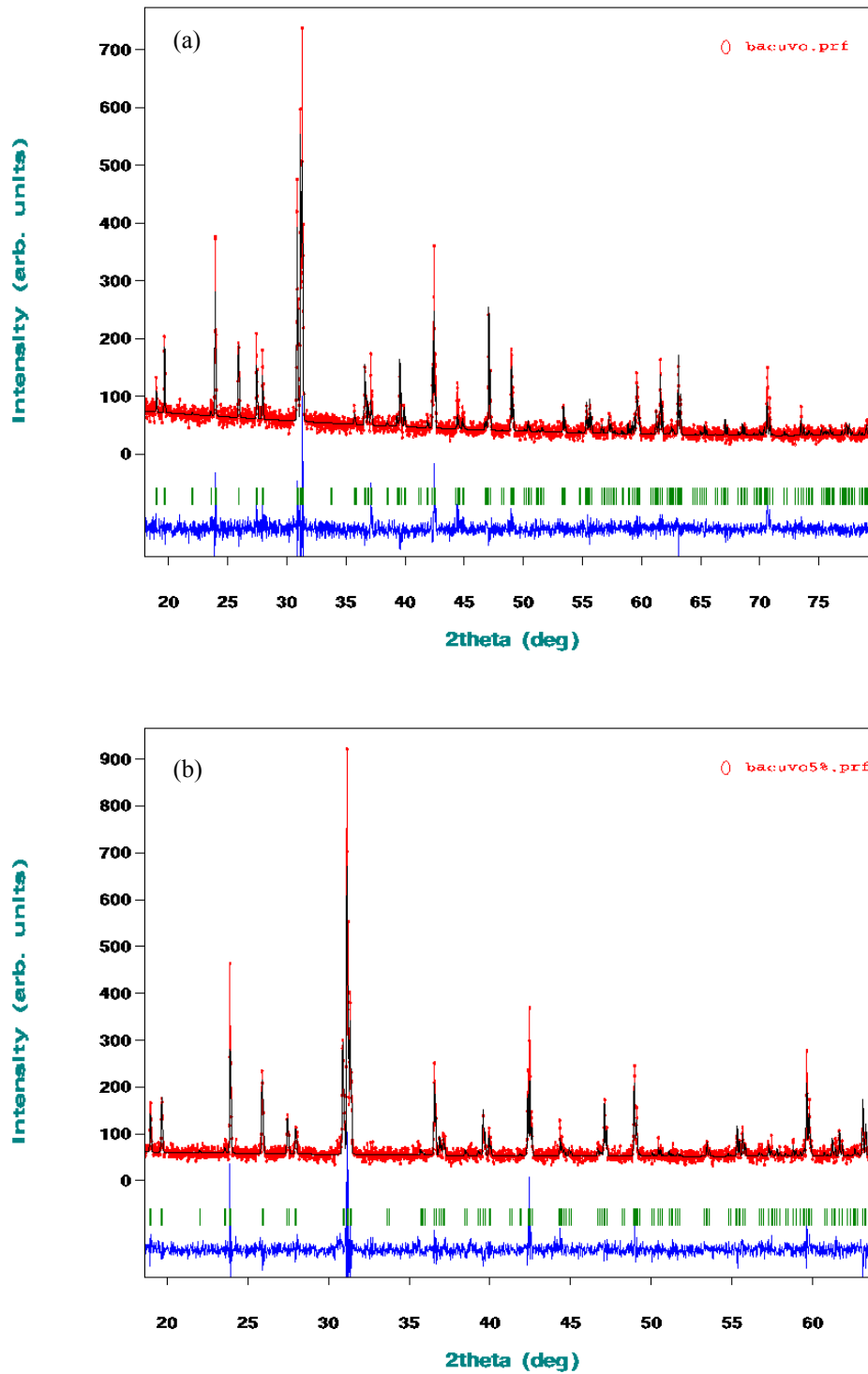


Figure 4.7 XRD diffraction profile of $\text{Ba}(\text{Cu}_{1-x}\text{Zn}_x)_2\text{V}_2\text{O}_8$ (a) $x=0$ and (b) $x=0.05$. Observed (red dots), calculated (solid line), and difference (blue). The vertical lines show the reflection positions.

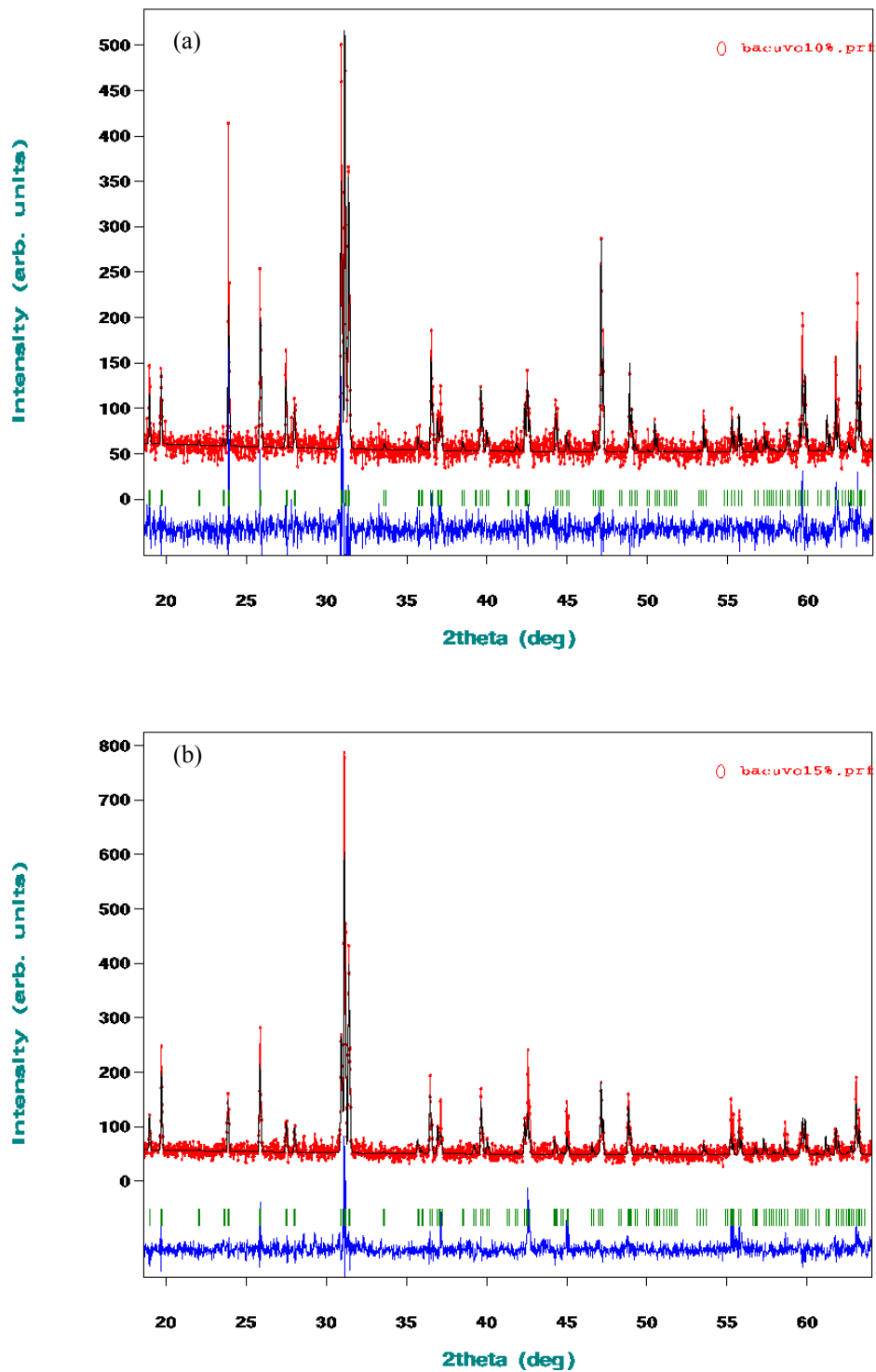


Figure 4.8 XRD diffraction profile of $\text{Ba}(\text{Cu}_{1-x}\text{Zn}_x)_2\text{V}_2\text{O}_8$ (a) $x=0.1$ and (b) $x=0.15$. Observed (red dots), calculated (solid line), and difference (blue). The vertical lines show the reflection positions

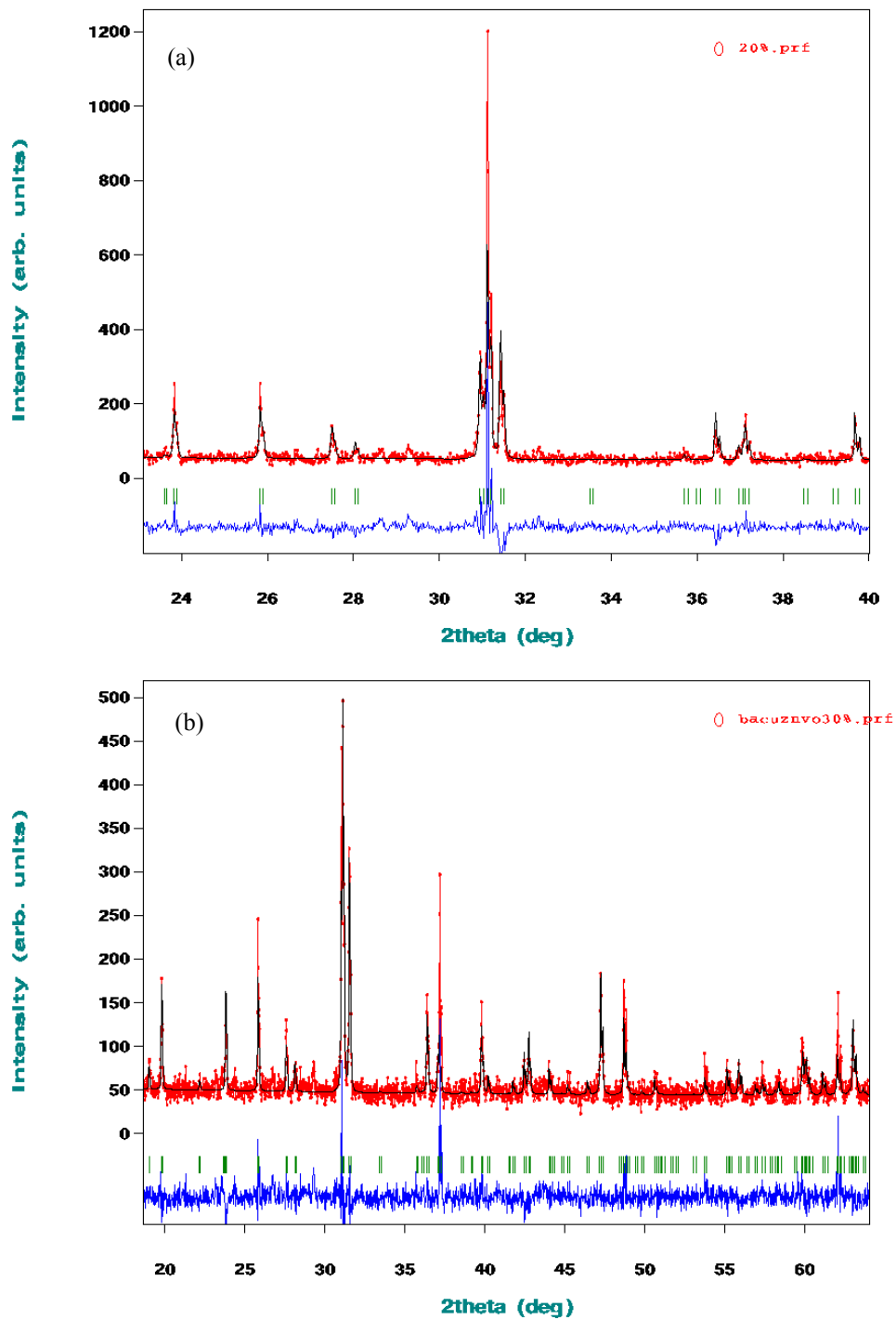


Figure 4.9 .XRD diffraction profile of $\text{Ba}(\text{Cu}_{1-x}\text{Zn}_x)_2\text{V}_2\text{O}_8$ (a) $x=0.2$ and (b) $x=0.3$. Observed (red dots), calculated (solid line), and difference (blue). The vertical lines show the reflection positions

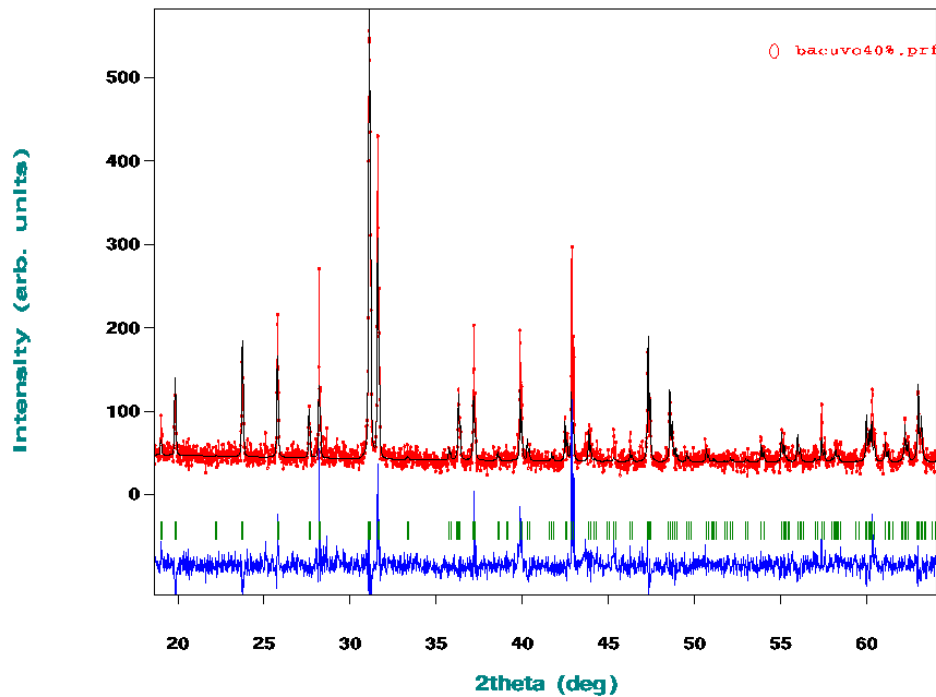


Figure 4.10 .XRD diffraction profile of $\text{Ba}(\text{Cu}_{1-x}\text{Zn}_x)_2\text{V}_2\text{O}_8$ $x=0.4$. Observed (red dots), calculated (solid line), and difference (blue). The vertical lines show the reflection positions

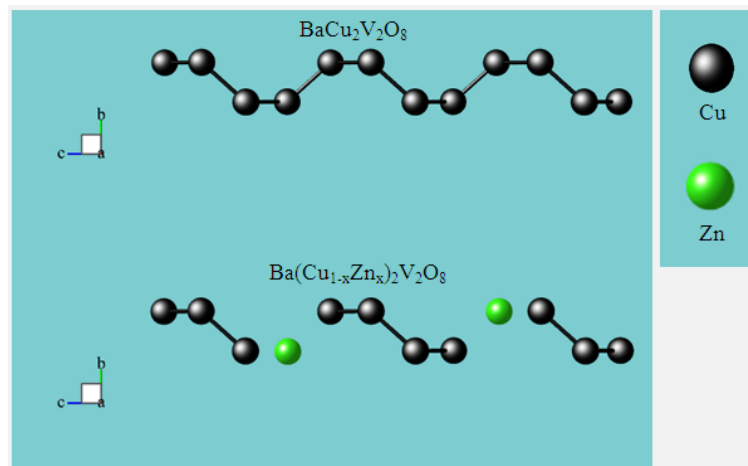


Figure 4.11 Effect of zinc doping on the spin chain. Zn^{2+} ions (spin 0) replace Cu^{2+} ions (Spin $\frac{1}{2}$) along the chain. The spin vacancies break the magnetic interactions in the chain.

4.3 Crystal growth of $\text{BaCu}_2\text{V}_2\text{O}_8$

Single crystals of $\text{BaCu}_2\text{V}_2\text{O}_8$ were prepared using two methods, the slow cooling method and the Bridgman-Stockbarger method. In the first step 5mol% V_2O_5 was mixed together with the $\text{BaCu}_2\text{V}_2\text{O}_8$ polycrystalline sample. This is in accordance with the results of He *et al.* [24] which show that using 5mol% V_2O_5 as self flux is favourable to the crystal growth.

4.3.1 The slow cooling method

The slow cooling method is made by melting the compound then cooling slowly through the melting point. For congruently melting materials (materials that maintain the same composition on melting). This will result in spontaneous nucleation (formation of a crystal) and crystal growth processes, if nucleation rates are slow and the growth is rapid, large crystals will result. Several trials were made in order to find the cooling rate that result in large crystals. The cooling rate has to be fast enough in order not to allow many nucleations to occur, and at the same time slow enough for the crystal growth process.

The following are the steps used for the crystal growth of $\text{BaCu}_2\text{V}_2\text{O}_8$ in the slow cooling method:

1. The mixture was placed in a quartz crucible and heated in the horizontal furnace at the rate 250°C degrees per hour, this allows the mixture to heat gradually to the temperature above its melting point $\sim 762^\circ\text{C}$

2. The mixture was kept at constant temperature $\sim 762^\circ\text{C}$ for several hours to ensure that the mixture is completely melted. For this step a few trials were made, for ~ 20 hours time period of constant temperature the sample was completely melted but a chemical reaction of the mixture with the quartz crucible was also occurring. A time period of ~ 6 hours of constant temperature was sufficient for the mixture to melt completely without significant reaction with the quartz crucible.

3. The mixture was cooled to room temperature at a rate of 0.5 degrees per hour. The slow cooling rate is chosen in order to keep nucleation rate low and at the same time to allow enough time for the crystal growth process.

4. The crucible was wrapped with a sheet of paper and gently broken with a hammer in order to separate the crucible material from the sample and to separate

single crystals from the rest of the solid compound. Small single crystals $\sim 0.5\text{mm}^3$ of $\text{BaCu}_2\text{V}_2\text{O}_8$ were collected.

4.3.2 The Bridgman-Stockbarger method

The Bridgman-Stockbarger method involves heating powder material above its melting point and slowly cooling it from one end of its container, where a seed crystal is located. The seed crystal can be placed prior to the melting or it can be formed by spontaneous nucleation at the end of the container which has a conical shape [Fig 4.12], the low volume of the tip ensures that only few nucleations will be formed at the bottom of the crucible. A single crystal of the same crystallographic orientation as the seed material is grown on the seed and is progressively formed along the length of the container. The process can be carried out in a horizontal or vertical geometry, for example by lowering the container through a temperature gradient (Stockbarger method)

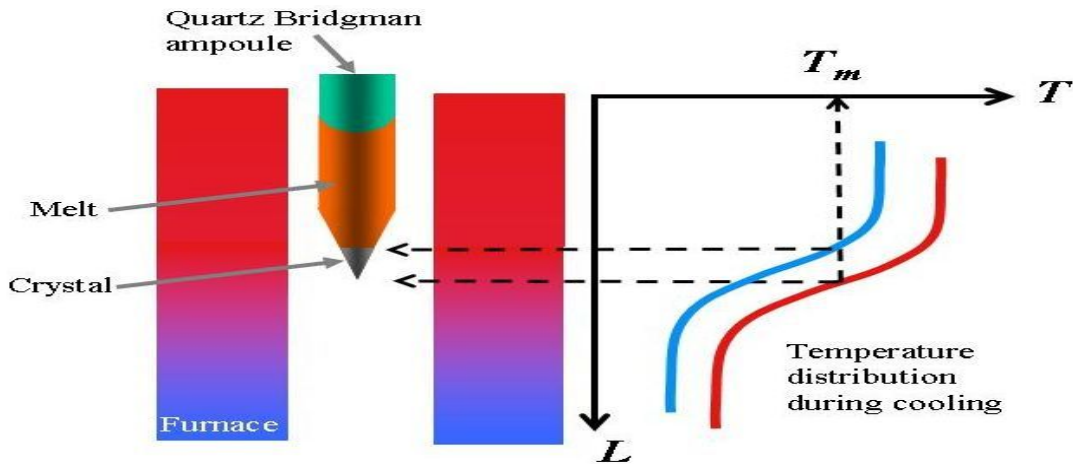


Figure 4.12 Bridgman-Stockbarger method: lowering the container through a temperature gradient.

Several trials using the Bridgman-Stockbarger method were used in order to find the best combinations of temperature gradient, lowering rate, furnace settings and crucible material/volume. The following are the steps used for the crystal growth of $\text{BaCu}_2\text{V}_2\text{O}_8$ in the Bridgman-Stockbarger method that resulted in the largest single crystals:

1. The mixture was placed in a quartz crucible with a conical shaped end and radius 5.5mm, so that it filled about 6cm of the quartz tube. These dimensions are chosen in order to have a large enough volume of mixture where single crystals can form.

2. The crucible was placed in the Bridgman furnace [Fig 4.14] with the settings described below. The lower tip of the tube was placed slightly above (0.5cm) the melting point temperature $\sim 760\text{C}^0$ according to the temperature profile of the furnace [Fig 4.13].

3. The crucible was lowered using the motor at the rate 0.5cm per day for a total of 12 days. So that the entire length of the mixture went through the melting point.

4. The furnace was cooled down to room temperature and the crucible was removed.

5. The crucible was wrapped with a sheet of paper and gently broken with a hammer in order to separate the crucible material from the sample and to separate single crystals from the rest of the solid compound. Small single crystals $\sim 1.5\text{mm}^3$ of $\text{BaCu}_2\text{V}_2\text{O}_8$ were collected [Fig 4.15].

6. The same process was repeated with a platinum crucible [Fig 4.2.b] filled to about 3 cm. The crucible was lowered for a total time of 6 days

4.3.2.1 Furnace settings

The furnace [Fig 4.13] was left open from the bottom and sealed from the top with thermal wool with only a small hole to allow for the sample rod to be lowered. This created a temperature gradient which was measured by lowering a thermocouple through the furnace [Fig 4.14].

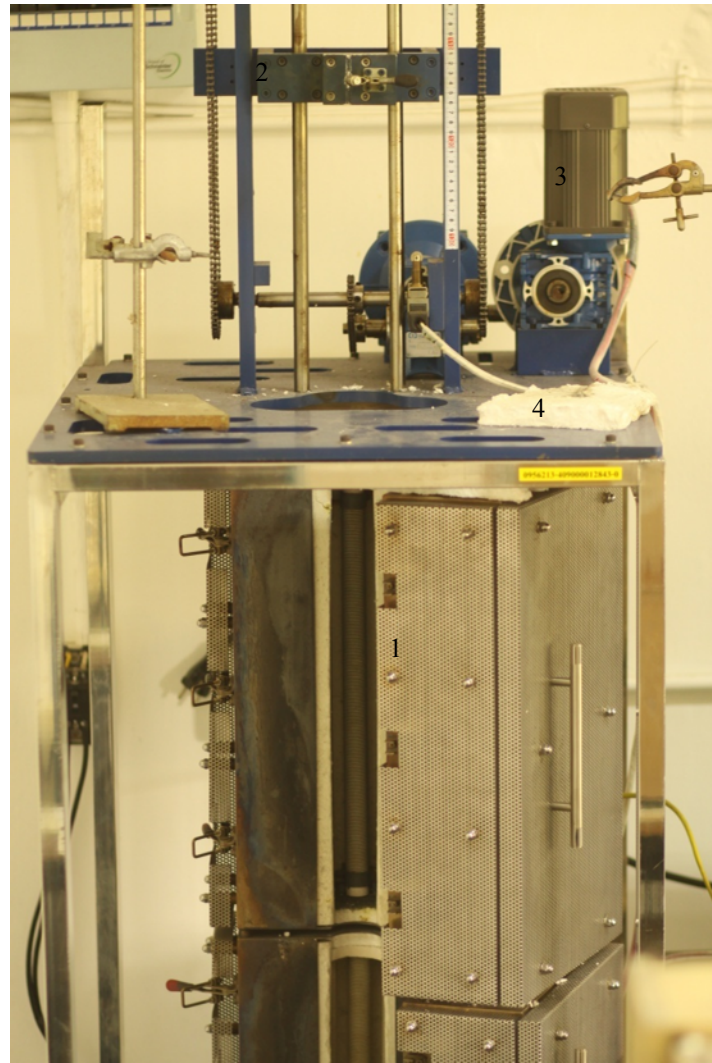


Figure 4.13 Furnace used for the Bridgman-Stockbarger method. (1) The furnace, (2) sample rod holder, (3) motor for lowering the sample, (4) thermal wool for sealing the top of the furnace. Bottom of furnace is left open.

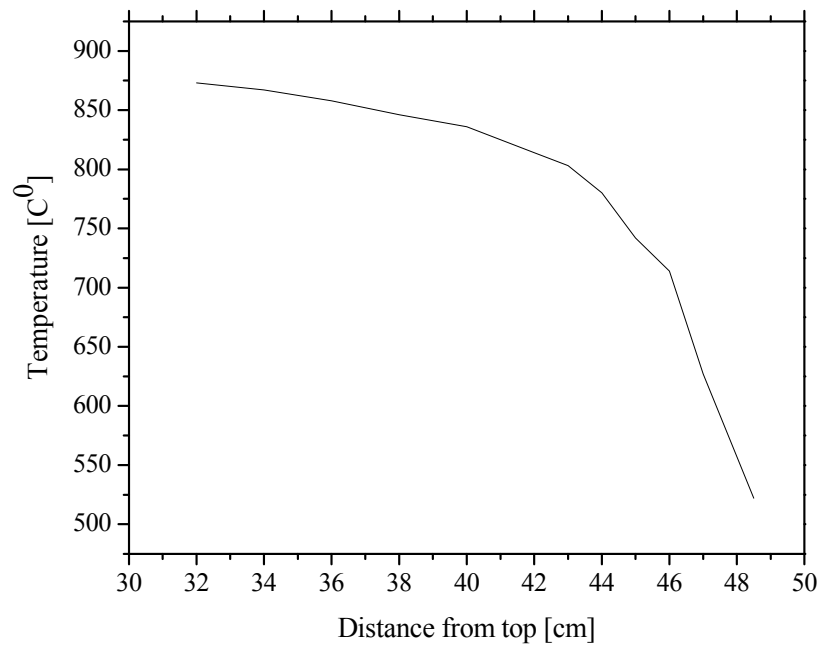


Figure 4.14 Temperature profile of the furnace.



Figure 4.15 Single crystal of $\text{BaCu}_2\text{V}_2\text{O}_8$ with dimension $\sim 1.5\text{mm}^3$

CHAPTER V

SUSCEPTIBILITY MEASUREMENT

5.1 Susceptibility measurement

The magnetization M as function of temperature T was measured for polycrystalline samples of $\text{Ba}(\text{Cu}_{1-x}\text{Zn}_x)_2\text{V}_2\text{O}_8$ ($x = 0, 0.05, 0.1$) using SQUID at constant applied field of $H=1$ Tesla. At this field the XXZ chain is expected to be in the Neel phase (for $J=41$ Mev, $\mu_B H/J \approx 3.1 \cdot 10^{-3}$, see chapter 1.3.1). The measurements were used to plot the susceptibility $\chi=M/H$, in the range T from 5K to 320K.

5.1.1 Sample preparation

Each of the three samples of $\text{Ba}(\text{Cu}_{1-x}\text{Zn}_x)_2\text{V}_2\text{O}_8$ ($x = 0, 0.05, 0.1$) was prepared using the following steps:

1. A small piece of teflon tape was cut and weighted using a scale [Table 5.1].
2. A few milligrams of sample were placed on the teflon and the total weight (teflon+ sample) was recorded [Table 5.1].
3. The teflon was wrapped around the sample and sealed inside a small capsule. The total weight (teflon+sample+capsule) was recorded [Table 5.1].
4. The capsule was inserted into a plastic straw [Fig 5.1].
5. The straw was mounted to the end of the sample rod [Fig 2.4] and put into the sample chamber.

Table 5.1 Weight of prepared samples.

Weight of sample $\text{Ba}(\text{Cu}_{1-x}\text{Zn}_x)_2\text{V}_2\text{O}_8$	Weight of teflon[mg]	Weight of teflon+ sample[mg]	Weight of teflon+ sample+capsule[mg]	Sample's weight[mg]
x=0	18.53	59.35	88.35	40.82
x=0.05	28.32	89.10	120.70	60.78
x=0.1	25.63	59.37	90.47	33.74

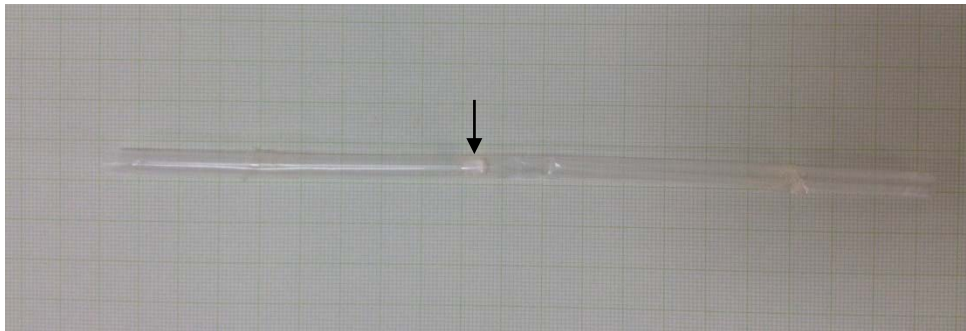


Figure 5.1 Capsule with powder sample inserted into a plastic straw.

5.1.2 Measurement process

After each sample was placed into the sample chamber, the magnetization as function of temperature was measured using the following steps:

1. The sample was centered using the automated process.
2. The sample was cooled down to 5K.
3. The applied magnetic field was set to 1Tesla.
4. The magnetization was measured at 5K steps up to the final temperature 320K.
5. For the x=0 and x=0.1 samples, the magnetization was measured at 5K steps as the sample was cooled back down to 5K

An additional measurement was performed in order to determine the background due to the teflon and capsule. A piece of teflon with weight 21.02mg was put inside a capsule so that the total weight (teflon+capsule) is 46.80mg. The measurement was performed using the same steps (1-4) as for all samples.

5.2 Measurement results

The results of the measurement for all samples were plotted in the following graphs.

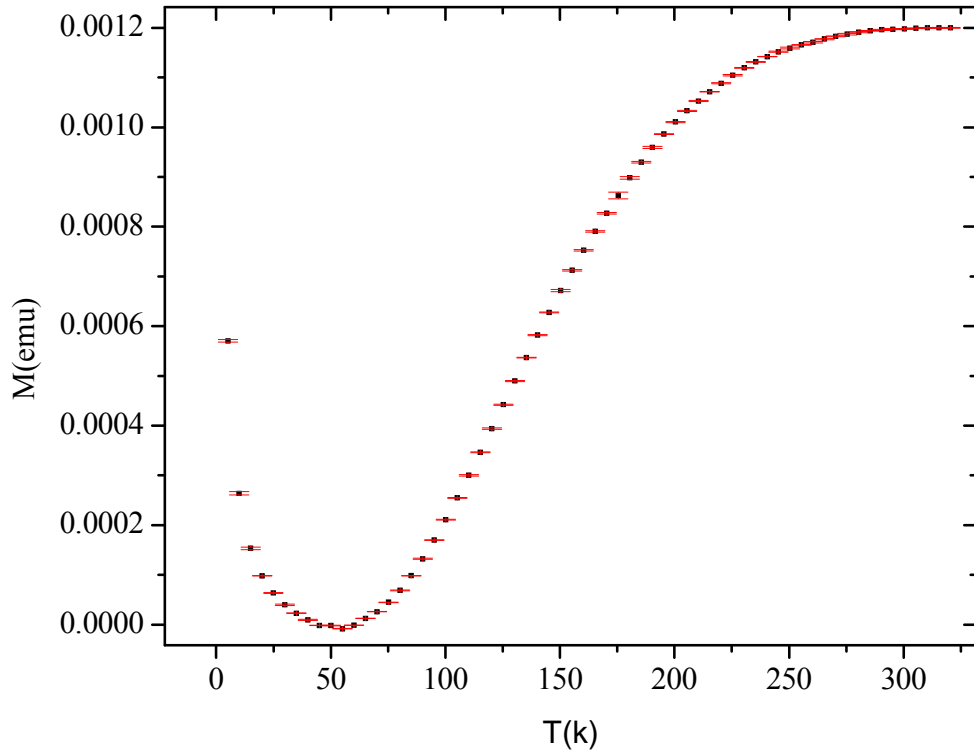


Figure 5.2 Measurement results for $\text{Ba}(\text{Cu}_{1-x}\text{Zn}_x)_2\text{V}_2\text{O}_8$ ($x = 0$). Magnetization (black dots) with error bars (red bars) which are $3 \times$ (standard deviation). In the temperature range 5-320K.

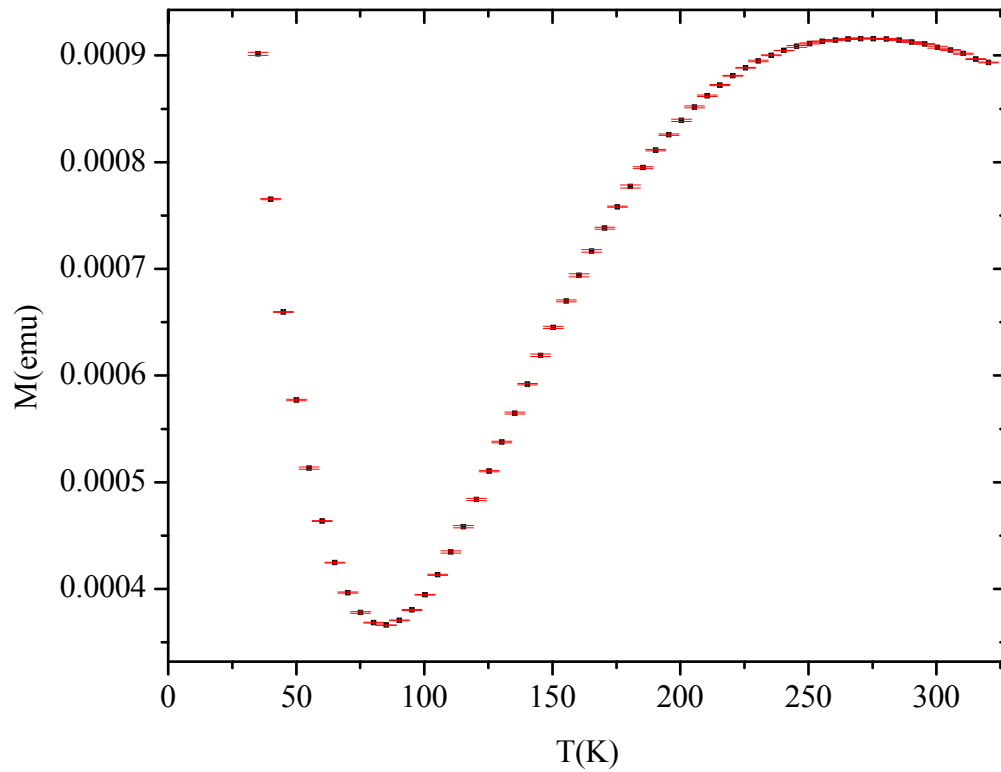


Figure 5.3 Measurement results for $\text{Ba}(\text{Cu}_{1-x}\text{Zn}_x)_2\text{V}_2\text{O}_8$ ($x = 0.05$). Magnetization (black dots) with error bars (red bars) which are $3 \times$ (standard deviation). In the temperature range 5-320K.

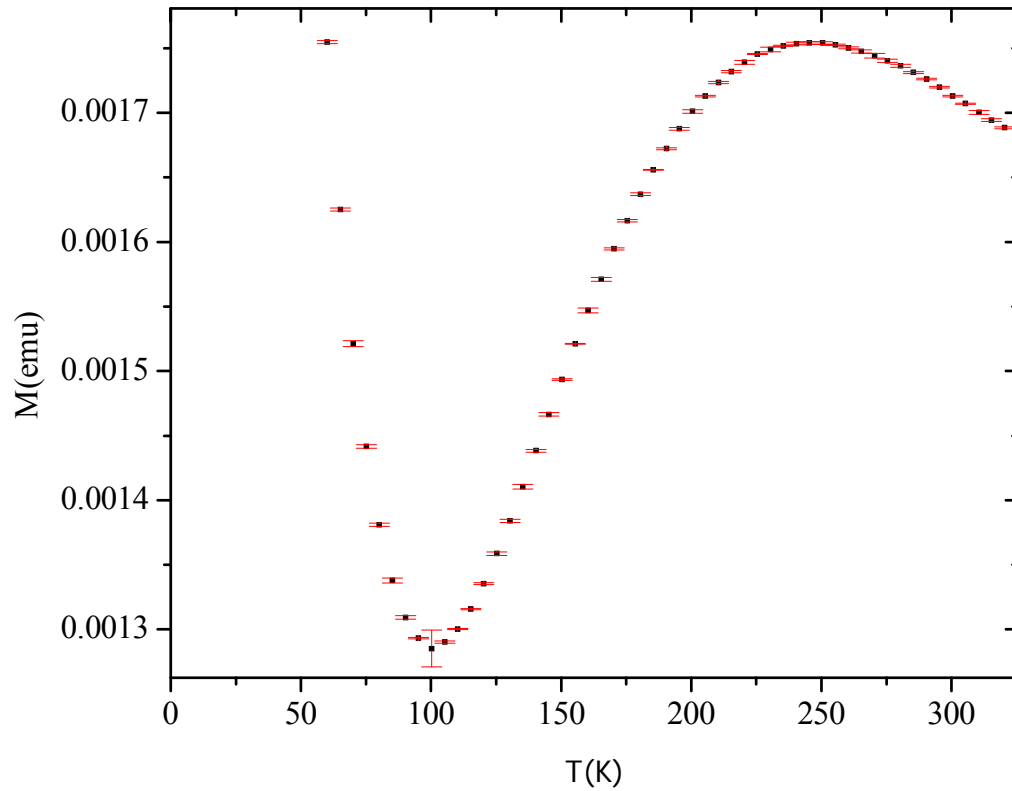


Figure 5.4 Measurement results for $\text{Ba}(\text{Cu}_{1-x}\text{Zn}_x)_2\text{V}_2\text{O}_8$ ($x = 0.1$). Magnetization (black dots) with error bars (red bars) which are $3 \times$ (standard deviation). In the temperature range 5-320K.

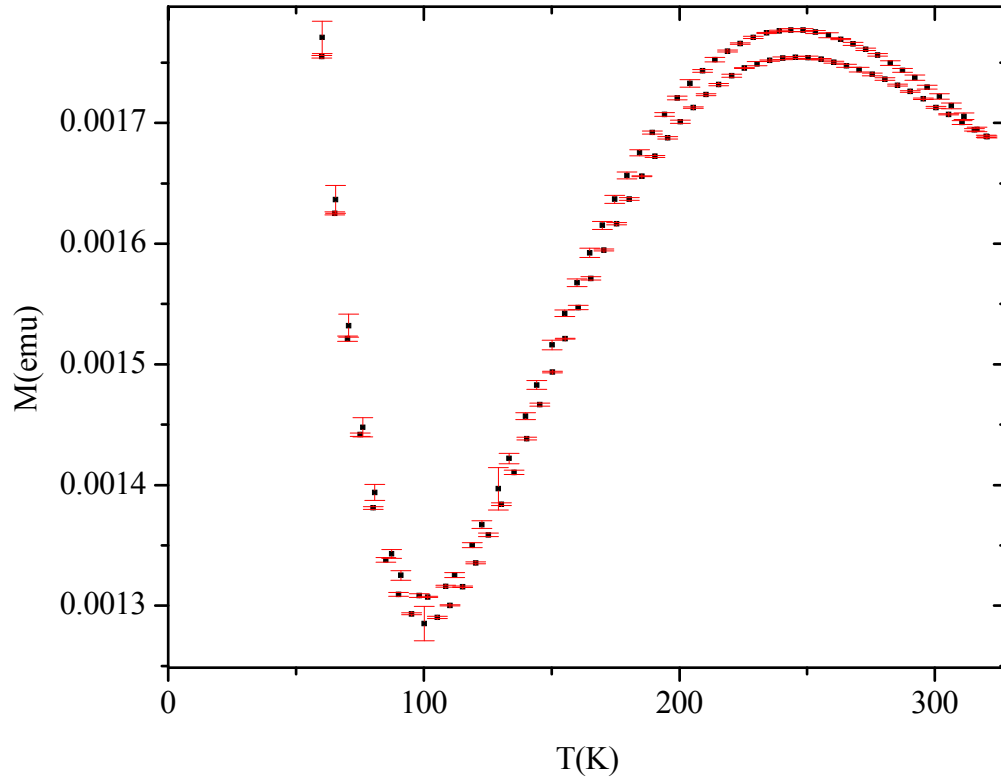


Figure 5.5 Measurement results for $\text{Ba}(\text{Cu}_{1-x}\text{Zn}_x)_2\text{V}_2\text{O}_8$ ($x = 0.1$). Magnetization (black dots) with error bars (red bars) which are $3 \times$ (standard deviation). In the temperature range 5-320K (bottom line) and 320-5K (top line).

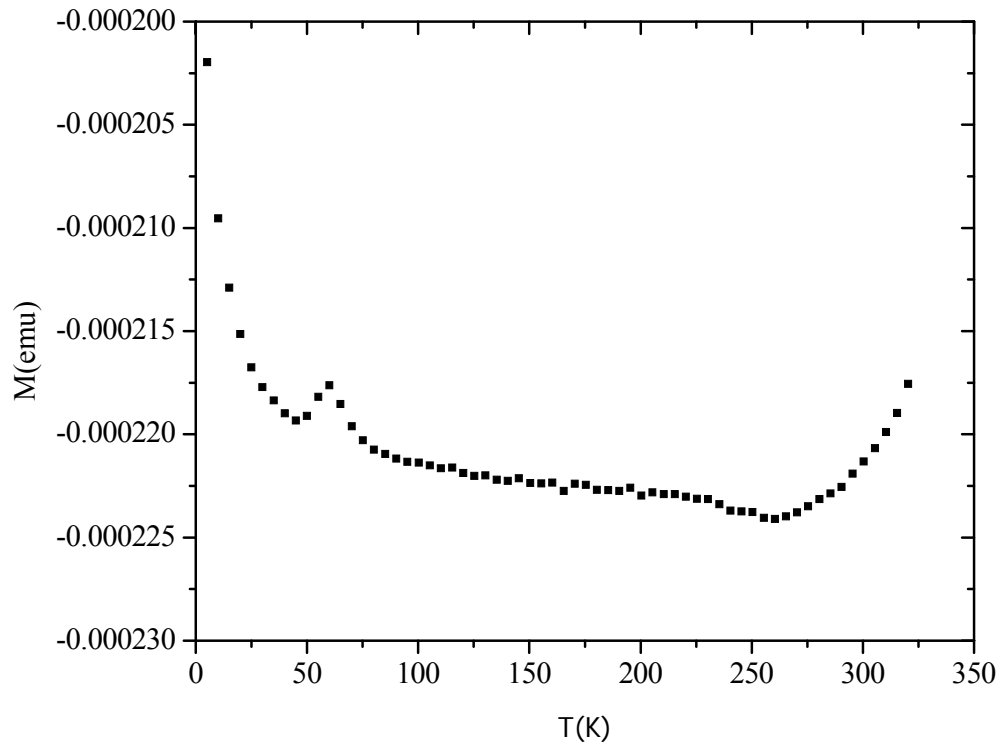


Figure 5.6 Measurement results for the background (teflon+capsule). Magnetization (black dots) in the temperature range 5-320K. Negative magnetization values due to teflon diamagnetism.

5.3 Data analysis

In this section the magnetization data for the three samples $\text{Ba}(\text{Cu}_{1-x}\text{Zn}_x)_2\text{V}_2\text{O}_8$ ($x = 0, 0.05, 0.1$) in the temperature range 5-320K (measurement from low to high temperature only) is analyzed. In order to plot the susceptibility as function of temperature, the background was first subtracted from each sample magnetization. Since each measurement contains a different amount of teflon the background was multiplied by the ratio of the teflon weight between sample and background measurements and later subtracted from the sample magnetization. After that the magnetization was divided by the value for the applied magnetic field (10000 Oe) in order to get the susceptibility $\chi = M/H$. For example the susceptibility for the $x=0$ sample was calculated:

$$\chi = \frac{M(\text{sample}) - M(\text{background}) \cdot \frac{21.02}{18.53}}{10000}$$

In addition, in order to get the susceptibility with units of mol Cu, the following calculation was used: each mol of formula contains 2 mol of Cu for the undoped ($x=0$) sample, 1.9 mol Cu for the 5% zinc doped sample ($x=0.05$) and 1.8 mol Cu for the 10% zinc doped sample ($x=0.1$). Each susceptibility measurement is multiplied by the grams per mol of the formula and divided by the sample weight [Table 5.1]. The susceptibilities calculations for the samples are summarized in the following table

Table 5.2 Calculation of the susceptibilities in units of mol Cu.

$\text{BaCu}_2\text{V}_2\text{O}_8$ ($x = 0$) 494.297 (g/mol)	$\chi^* = \chi \cdot \frac{494.297}{2 \cdot 40.82 \cdot 10^{-3}}$
$\text{BaCu}_{1.9}\text{Zn}_{0.1}\text{V}_2\text{O}_8$ ($x = 0.05$) 494.482 (g/mol)	$\chi^* = \chi \cdot \frac{494.482}{1.9 \cdot 33.74 \cdot 10^{-3}}$
$\text{BaCu}_{1.8}\text{Zn}_{0.2}\text{V}_2\text{O}_8$ ($x = 0.1$) 494.666 (g/mol)	$\chi^* = \chi \cdot \frac{494.666}{1.8 \cdot 60.78 \cdot 10^{-3}}$

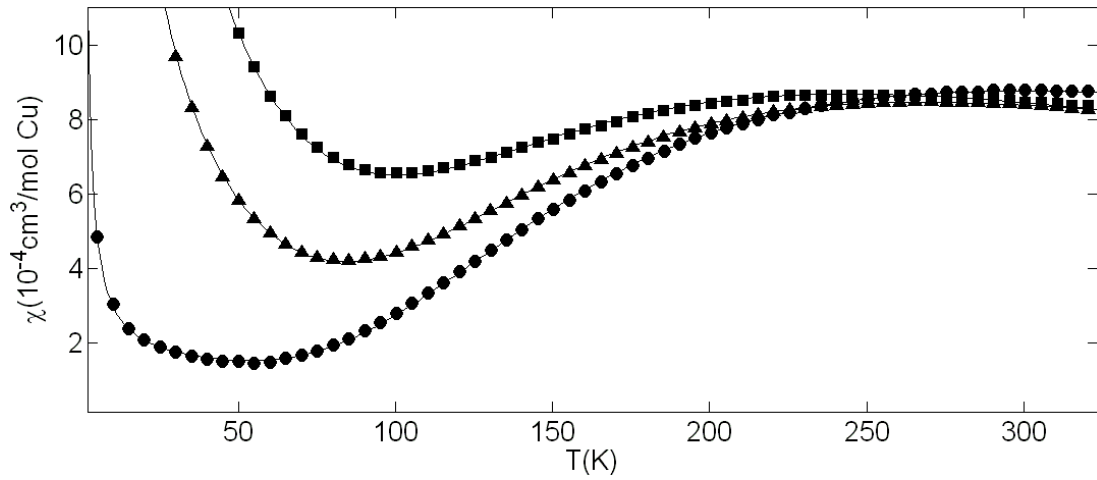


Figure 5.7 Temperature dependence of magnetic susceptibility of $\text{Ba}(\text{Cu}_{1-x}\text{Zn}_x)_2\text{V}_2\text{O}_8$, $x = 0$ (circles), 0.05 (triangles), and 0.1 (squares) from 5K to 320K. The solid lines represent the result of fitting to the equation $\chi(T) = \chi_0 + \chi_{\text{cw}}(T) + \chi_{\text{spin-dimer}}(T)$.

Plotting all three graphs of $\chi^*(T)$ together shows the effects of the zinc doping on the susceptibilities [Fig 5.7]. The plots for $\chi^*(T)$ were fitted with the following model using Matlab.

$$\chi(T) = \chi_0 + \chi_{\text{cw}}(T) + \chi_{\text{spin-dimer}}(T),$$

where χ_0 is the temperature independent term, $\chi_{\text{cw}}(T) = C / (T - \Theta)$ is the Curie-Weiss term which models the upturn below 60K, and $\chi_{\text{spin-dimer}}(T) = Ng^2 \mu_B^2 / [k_B T (3 + e^{J/k_B T})]$, (see chapter 1.5) The results of the fit are summarized in Tables 5.3, 5.4 and 5.5

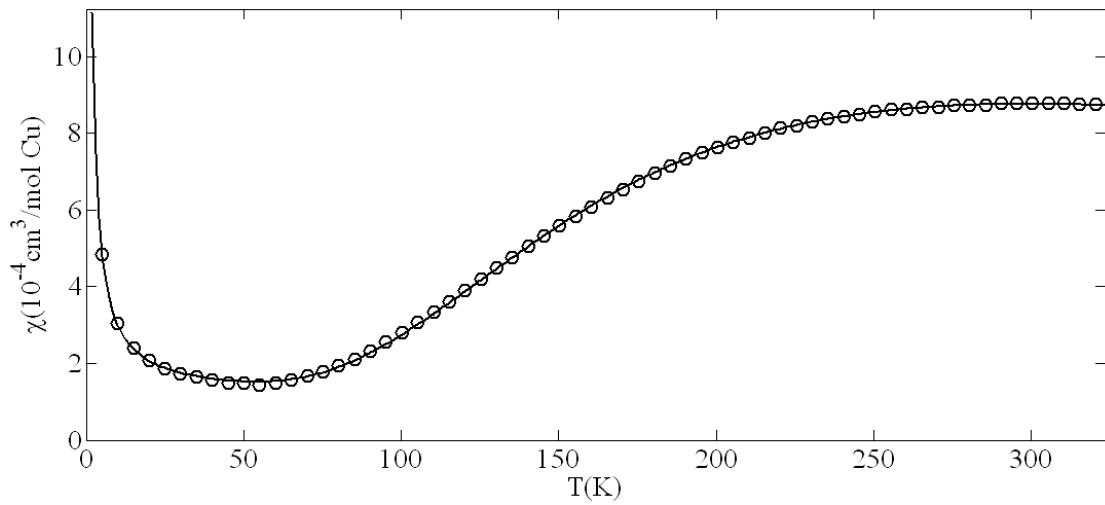


Figure 5.8 Temperature dependence of magnetic susceptibility of BaCu₂V₂O₈ (open circles) with a fit (solid line) to the isolated dimer model. R²=0.9999.

Table 5.3 Fitted results for the isolated dimer model for BaCu₂V₂O₈ (x = 0).

Parameter	Fitted value	Error (range)
χ_0	0.000113	(0.00011, 0.000116)
C	0.001868	(0.001756, 0.00198)
Θ	0.03802	(-0.2545, 0.3305)
$Ng^2\mu_B^2$	1.816	(1.809, 1.823)
J/k_B	482.4	(481.2, 483.7)

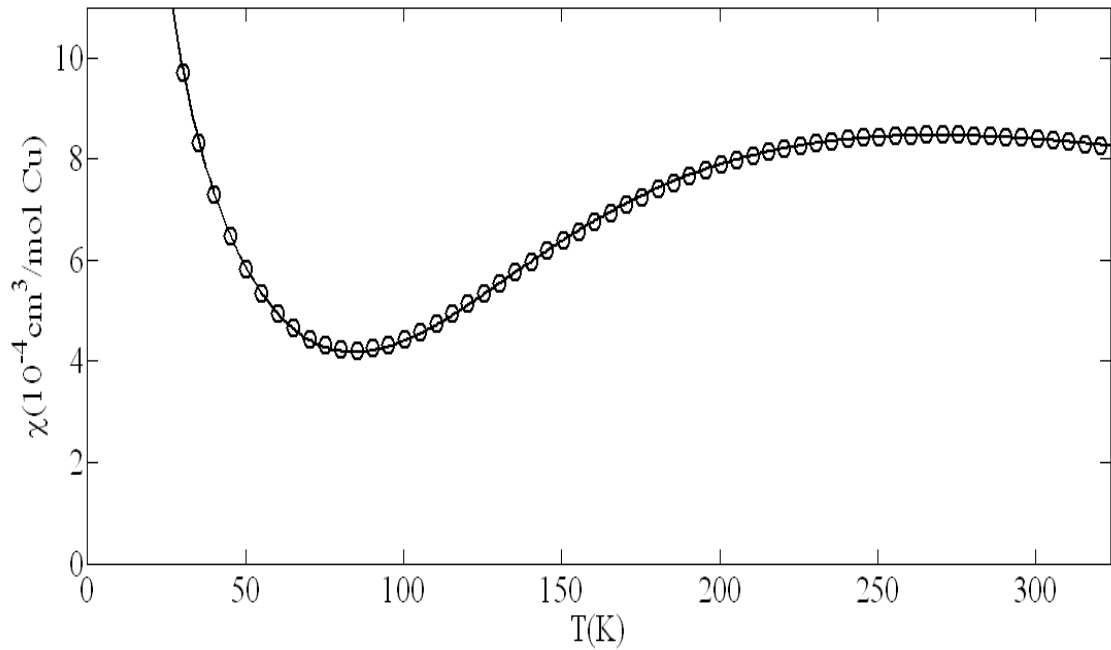


Figure 5.9 Temperature dependence of magnetic susceptibility of $\text{Ba}(\text{Cu}_{1-x}\text{Zn}_x)_2\text{V}_2\text{O}_8$ ($x=5$) (open circles) with a fit (solid line) to the isolated dimer model.

Table 5.4 Fitted results for the isolated dimer model for $\text{Ba}(\text{Cu}_{1-x}\text{Zn}_x)_2\text{V}_2\text{O}_8$ ($x=5$).

Parameter	Fitted value	Error (range)
χ_0	-2.13e-005	(-2.701e-005, -1.558e-005)
C	0.03048	(0.03026, 0.0307)
Θ	-0.4105	(-0.4501, -0.3709)
$Ng^2\mu_B^2$	1.771	(1.759, 1.783)
J/k_B	469.3	(467.1, 471.5)

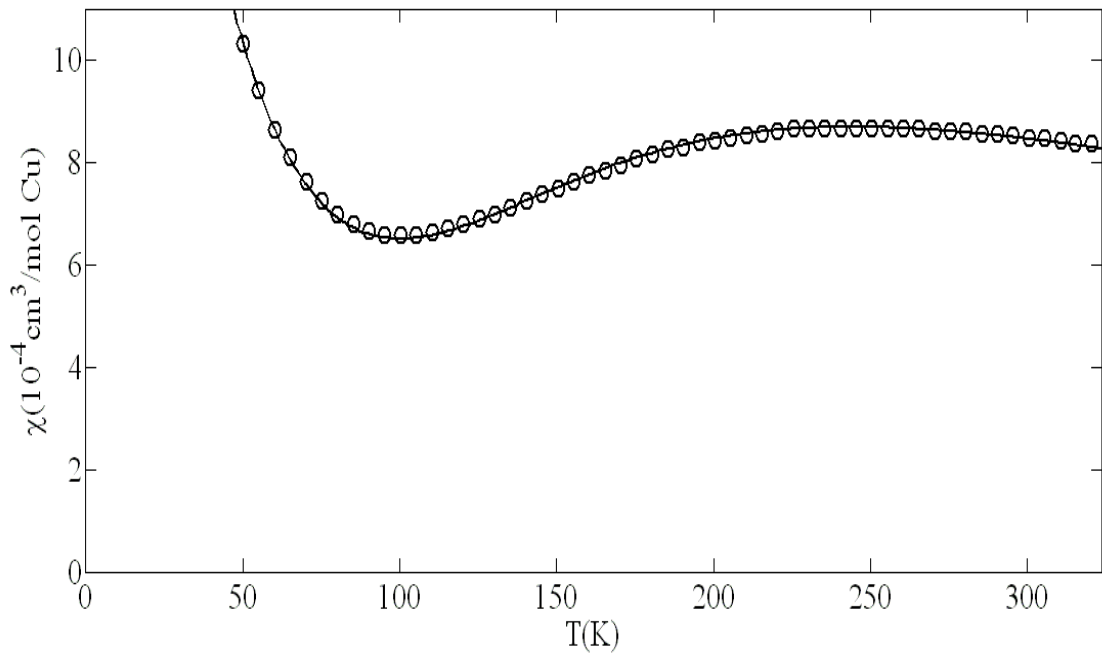


Figure 5.10 Temperature dependence of magnetic susceptibility of $\text{Ba}(\text{Cu}_{1-x}\text{Zn}_x)_2\text{V}_2\text{O}_8$ ($x=10$) (open circles) with a fit (solid line) to the isolated dimer model.

Table 5.5 Fitted results for the isolated dimer model for $\text{Ba}(\text{Cu}_{1-x}\text{Zn}_x)_2\text{V}_2\text{O}_8$ ($x=10$).

Parameter	Fitted value	Error (range)
χ_0	-3.48e-005	(-4.262e-005, -2.697e-005)
C	0.05357	(0.05327, 0.05387)
θ	-0.1944	(-0.2235, -0.1653)
$Ng^2\mu_B^2$	1.626	(1.609, 1.642)
J/k_B	465.4	(462.1, 468.6)

To see the susceptibility which is due to only the spin exchange, the Curie term was subtracted from the susceptibility of $\text{BaCu}_2\text{V}_2\text{O}_8$ [Fig 5.8] using the fit result for the Curie parameter [Table 5.3].

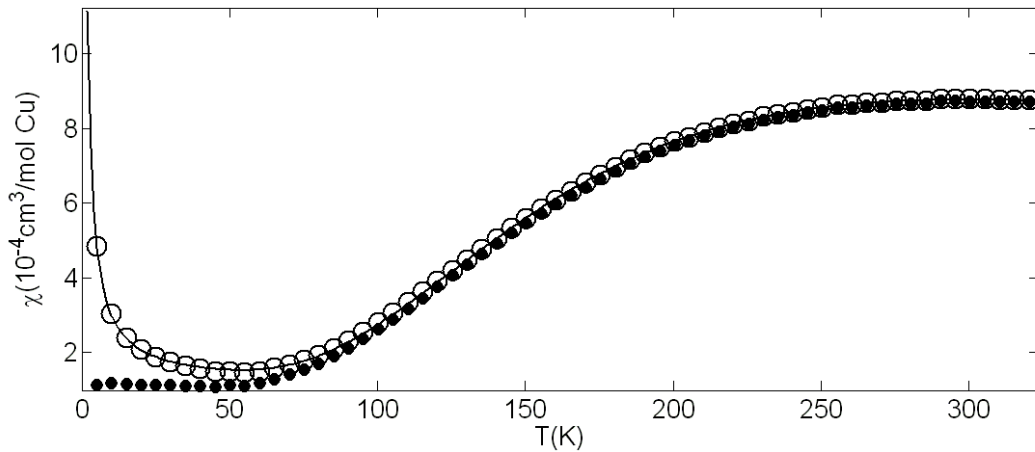


Figure 5.11 Temperature dependence of magnetic susceptibility of $\text{BaCu}_2\text{V}_2\text{O}_8$ (open circles) with a fit (solid line) to the isolated dimer model. Filled circles are the data after subtraction of the fitted Curie term.

5.3.1 Fit to the alternating chain model

The data were also fitted to the alternating chain model [see Chapter 1.5]. The following Matlab [Fig 5.12] script was written in order to simulate the models for the susceptibility data. It is noted that for $\alpha=0$ the alternating chain model is identical to the isolated dimer model from the previous section. A comparison to the simulated results for low values of α (the gap value is set $\Delta=482.4\text{K}$) is also plotted [Fig 5.13]. The result of fitting the model with the data show that the best fit is achieved when $\alpha=0$ for all samples (doped and undoped). Fitting the data for both parameters α and J , at the same time and forcing $\alpha \neq 0$, results in the best fit for $\alpha=0.2$ and $\Delta=416\text{K}$. This fit is not as good at the fit to the isolated dimer model as can be seen from lower values of R^2 and from the examination of the plot [Fig 5.14].

```

% S=1/2 alternating AF chain susceptibility, to be used with fitvar file
% c: alpha(alternation parameter) , b: Jmax/Kb , a: N(g^2)(Mb^2)/4Kb ,
% to: weiss temp , imp: Nimp , xo=zero susceptibility
df=1-(0.5*c)-(2*(c^2))+((3/2)*c^3); % delta fit parameter
d0=((1-c)^(3/4))*((1+c)^(1/4))+g1*c*(1-c)+(g2*(c^2)*((1-c)^2)); % delta zero parameter
for j=1:6 %Nn
    NN(1,j)=0;
    for i=0:4
        NN(1,j)=NN(1,j)+N(j,i+1)*(c^i);
    end
end
for j=1:7 %Dn
    DD(1,j)=0;
    for i=0:4
        DD(1,j)=DD(1,j)+D(j,i+1)*(c^i);
    end
end

pm11=1+(((N(7,2)*c+N(7,3)*c^2).*(d0.*(b./t).^y).*(b./t).^7));
pm12=0;
for i=1:6
    pm12=pm12+NN(1,i).*(b./t.^i);
end
pm1=pm11+pm12; % Pm nominator

pm21=1+(((D(8,2)*c+D(8,3)*c^2).*(d0.*(b./t).^z).*exp((d0-df).*(b./t)).*(b./t).^8));
pm22=0;
for i=1:7
    pm22=pm22+DD(1,i).*(b./t.^i);
end
pm2=pm21+pm22; %Pm denominator

pm=pm1./pm2;
e=(exp(-df.*(b./t))).*(a./t);
%e=(exp(-df.*(1./t.*kb))).*(a./t);
s=e.*pm; % complete function
%plot(t,s);
cw=(imp*a)./(t-to); % currie weiss term 0.1% impurity
ss=s+cw+xo; % full fit
%figure(2)
%plot(t,ss);
figure(3)
plot(t,ss,bacuvo(1:64,1),bacuvo(1:64,2));

dimer=xo+cw+(exp(-b./t).*((4*a)/t)).*(1./(1+(3*exp(-1.*(b./t)))));
figure(4)
plot(t,dimer,t,ss); %dimer model vs alternating

```

Figure 5.12 Matlab script for the simulation of the alternating chain model and the dimer model. All parameters are inserted to the variable file (fitvar.mat) as well as the susceptibility data for the sample.

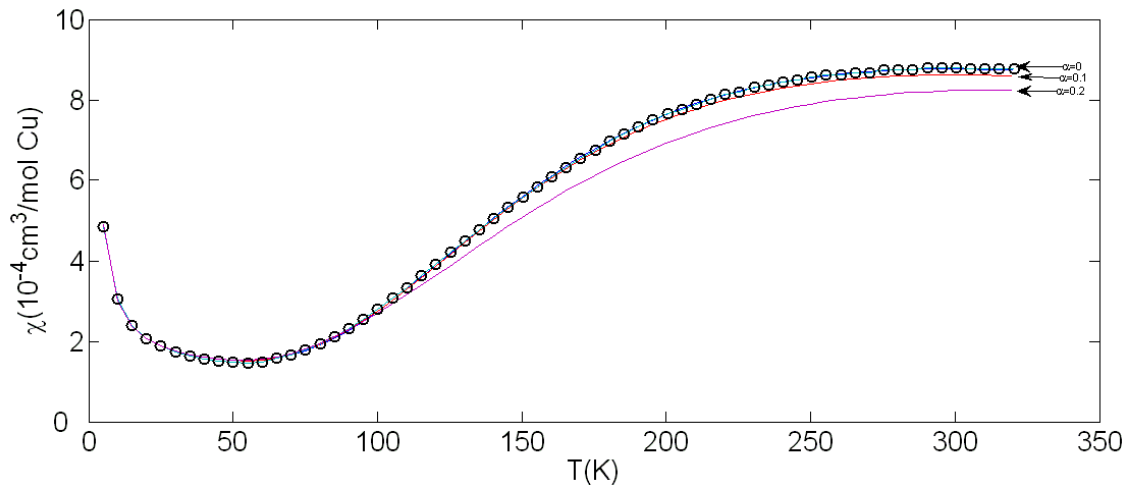


Figure 5.13 Fit of magnetic susceptibility of $\text{BaCu}_2\text{V}_2\text{O}_8$ (dots) to the alternating chain model with different value of alternation parameter α (lines). The gap is set to $\Delta=482.4\text{K}$

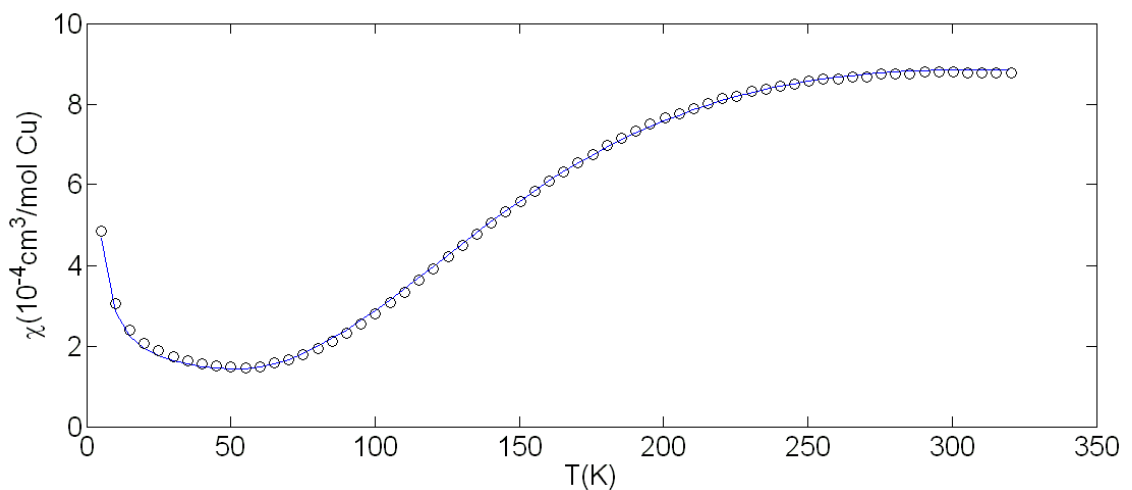


Figure 5.14 Fit of magnetic susceptibility of $\text{BaCu}_2\text{V}_2\text{O}_8$ (dots) to the alternating chain model with $\alpha=0.2$ and $\Delta=416\text{K}$. $R^2=0.9994$.

CHAPTER VI

DISCUSSION

6.1 Sample preparation

Polycrystalline samples of $\text{BaCu}_2\text{V}_2\text{O}_8$ and zinc doped samples of $\text{Ba}(\text{Cu}_{1-x}\text{Zn}_x)_2\text{V}_2\text{O}_8$ ($x= 0.05, 0.1, 0.15, 0.2, 0.3$ and 0.4) were prepared using the solid state reaction method, XRD measurements of samples with doping percentage up to 40% showed no impurity and gave a good fit to the structure file as can be seen from the low values of χ^2 [Table 4.3] which means that zinc was successfully substituted for copper [Fig 4.10]. The lattice parameters for each sample up to 40% were estimated from the peak positions in the diffraction pattern using the Reitveld refinement. The results show that the lattice parameter a linearly decreases and the lattice parameter c linearly increases with higher doping (x) [Fig 4.5,6]. Single crystals of $\text{BaCu}_2\text{V}_2\text{O}_8$ were prepared using two methods, the slow cooling method and the Bridgman-Stockbarger method using 5mol% V_2O_5 as self flux. The chemical reaction between sample and quartz crucible starts to occur at the melting point temperature. For the slow cooling method, a time period of ~ 6 hours of constant temperature was sufficient for the mixture to melt completely without significant reaction with the quartz crucible, however only very small single crystals $\sim 0.5\text{mm}^3$ were obtained. In the Bridgman-Stockbarger method both quartz and platinum crucibles were used, both gave similar results and small single crystals $\sim 1.5\text{mm}^3$ were obtained. Reaction between sample and quartz crucible was occurring in this method. However, the crystals were removed from the inner part of the crucible where the reaction was not significant. The single crystals obtained in this work are still much smaller than the reported results from He *et al.* [24] who grew high-quality large single crystals of with dimensions $25 \times 10\text{mm}$ by the top-seeded growth method.

6.2 Magnetic susceptibility of BaCu₂V₂O₈

The magnetization of BaCu₂V₂O₈ shows no hysteresis [Fig 5.2] and the magnetic susceptibility data [Fig 5.3] give a good fit ($R^2=0.9999$) to the isolated dimer model $\chi(T)=\chi_0+\chi_{cw}(T)+\chi_{spin-dimer}(T)$. A fit is also possible with an alternating chain model with $\alpha=0.2$ and $\Delta=416K$, however this results in a lower value for $R^2=0.9994$. A broad maximum is observed around 280K which is due to the low magnetic dimensionality (see Chapter 1.4). Below this broad maximum, the susceptibility decreases rapidly with decreasing temperature and an upturn appears below 60K which originates possibly from natural defects and/or small amounts of paramagnetic impurities, most likely due to isolated Cu ions. This upturn is modelled with the Curie-Weiss term:

$$\begin{aligned}\chi_{cw}(T) &= C / (T - \Theta) \\ C &= [\mu_B^2 g^2 J(J+1) N_{imp}] / 3k_B\end{aligned}\quad (6.1)$$

Where C is the Curie constant. $J=1/2$ is the angular momentum of the Cu ions and the number of impurities N_{imp} can be extracted from the fitted value of the Curie constant [Table 5.3]. The Lande g-factor is taken to be 2.2, a typical value for Cu in the crystalline environment. The Curie-Weiss constant Θ is approximately zero from the result of the fit as expected (no phase transition for $T>0$ for non interacting spins).

Subtracting the Curie term from the susceptibility [Fig 5.11] shows that the susceptibility decreases as the temperature goes to zero and reaches an approximately constant value for $T<60K$. This constant value (χ_0) can be attributed to the core diamagnetic susceptibilities for individual ions in BaCu₂V₂O₈, in addition to the Van Vleck paramagnetic susceptibility.

The susceptibility results are in agreement with the isolated dimer model, this suggests that the ground state is a spin singlet ($S_{tot}=0$) which explains the magnetization plateau in the range $T<60$ where $M=\chi_0 H$. As the temperature rises above $T>60$ the Cu dimers start to get excited to the triplet state ($S_{tot}=1$). After all dimers reach the triplet state the magnetization stays constant for the range $280K<T<320K$ which is the typical plateau for low magnetic dimensionality. The fit to the isolated dimer model gives an energy gap between the singlet ground state and the triplet state $\Delta/k_B=482K$. This result is in agreement with a similar study by Sarita *et al* [21].

6.3 Magnetic susceptibility of zinc doped $\text{Ba}(\text{Cu}_{1-x}\text{Zn}_x)_2\text{V}_2\text{O}_8$

The magnetic susceptibility data [Fig 5.9 and 10] give a good fit ($R^2=0.9999$) to the isolated dimer model $\chi(T)=\chi_0+\chi_{\text{cw}}(T)+\chi_{\text{spin-dimer}}(T)$, for both $x=0.05$ and $x=0.1$. The fitted values for the spin gap Δ [Table 6.1] are weakly dependent on x [Fig 6.1]. This result indicates that the spin vacancies have little effect on the interdimer interactions and the dimer pair is almost isolated, which suggests that the isolated dimer model is suitable for this system. The number of impurities N_{imp} can be extracted from the Curie constant (C). The percentage of impurity was calculated from $N_{\text{imp}}(\%)=N_{\text{imp}}/N_A$ where N_A is the Avogadro constant and the percentage of dimer pairs is $N(\%)=N/N_A$. The plot of parameters $N(\%)$ and $N_{\text{imp}}(\%)$ against x shows that $N(\%)$ decreases while $N_{\text{imp}}(\%)$ increases with x [Fig 6.2]. This is due to the substitution of copper with zinc which reduces the number of dimer pairs. The Curie-Weiss constant Θ is approximately zero for the undoped compound and has small values for the doped samples [Table 6.1], which could be the result of the increase in density of the unpaired copper ions which have weak interactions.

Table 6.1 Fit parameters for magnetic susceptibility data of $\text{Ba}(\text{Cu}_{1-x}\text{Zn}_x)_2\text{V}_2\text{O}_8$.

Parameter	$x=0$	$x=0.05$	$x=0.1$
Δ/k_B (K)	482.4 ± 1.3	469.3 ± 2.2	465.4 ± 3.3
Θ (K)	0.03802 ± 0.3	-0.4105 ± 0.04	-0.1944 ± 0.03
$N(\%)$	100.02 ± 0.39	97.5 ± 0.66	89.5 ± 0.94
$N_{\text{imp}}(\%)$	0.4 ± 0.07	6.7 ± 0.05	11.8 ± 0.02

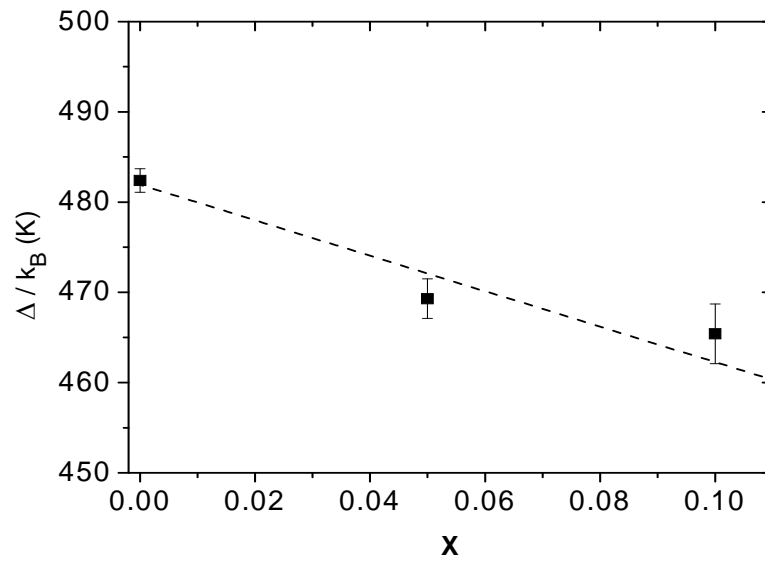


Figure 6.1 The dependence of the spin gap (Δ/k_B) on doping (x) of $\text{Ba}(\text{Cu}_{1-x}\text{Zn}_x)_2\text{V}_2\text{O}_8$ ($x = 0, 0.05, 0.1$). The broken line is a guide to the eye.

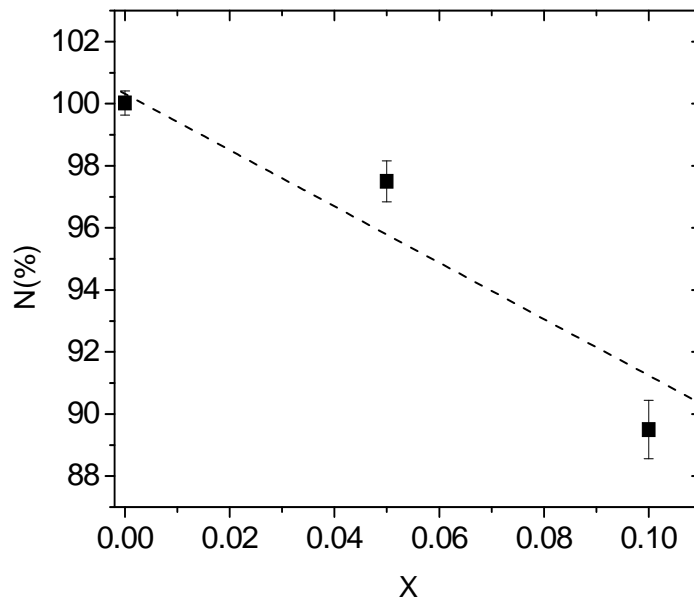


Figure 6.2 The dependence of $N(\%)$ on doping (x) of $\text{Ba}(\text{Cu}_{1-x}\text{Zn}_x)_2\text{V}_2\text{O}_8$ ($x = 0, 0.05, 0.1$). The broken line is a guide to the eye.

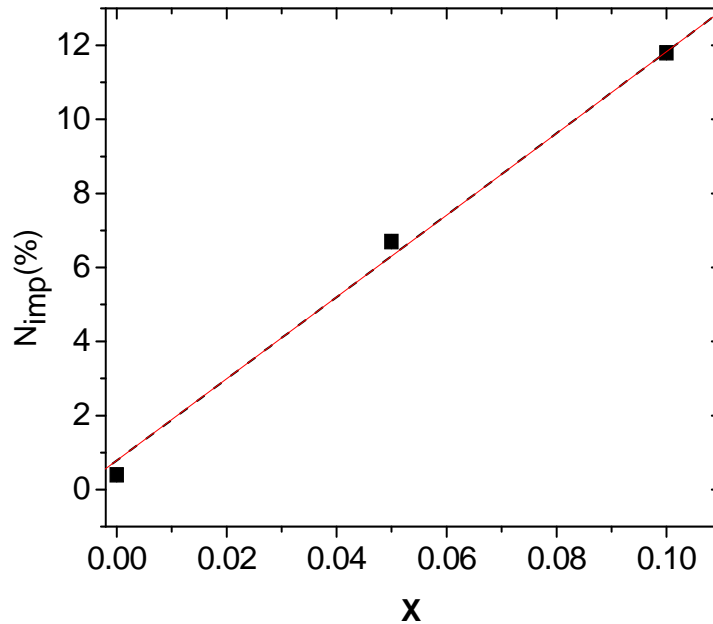


Figure 6.3 The dependence of $N_{imp}(\%)$ on doping (x) of $\text{Ba}(\text{Cu}_{1-x}\text{Zn}_x)_2\text{V}_2\text{O}_8$ ($x = 0, 0.05, 0.1$). With linear fit (solid line) to $N_{imp}(\%)=0.78+ 110.47x$.

6.4 Conclusion

The study of the one dimensional spin gap compound $\text{BaCu}_2\text{V}_2\text{O}_8$ was performed by means of magnetic susceptibility measurements on powder samples. The isolated dimer model gave a good fit to the data. The ground state is a spin singlet with an energy gap $\Delta/k_B = 482\text{K}$ due to dimerization of the chain. The effects of substituting zinc for copper on the spin gap were studied by means of susceptibility measurements of $\text{Ba}(\text{Cu}_{1-x}\text{Zn}_x)_2\text{V}_2\text{O}_8$ ($x = 0, 0.05, 0.1$). The results show that Δ is weakly dependent on x , which suggests that the spin vacancies have little effect on the interdimer interaction, hence the isolated dimer model is suitable for this system. Figures 6.4 and 6.5 illustrate the effect of the zinc doping in the alternating exchange and isolated dimer model. Zinc doping breaks the interaction along the chain, in the alternating exchange picture, the interdimer interaction will affect the excitation spectrum and the spin gap will depend strongly on doping amount. In the isolated dimer picture, the number of dimers reduces as the doping amount increases. The magnitude of the gap

for each dimer is unaffected. From the fit of the dimer model, the number of free spins N_{imp} increases with doping which is also an indication that the isolated dimer model is more suitable. The ratio between the percentage of impurity and doping is $N_{\text{imp}}(\%)/x(\%)=1.1$ [Fig 6.3]. In the alternating exchange picture, substituting zinc for copper does not cause a large amount of free spins to be formed in the chain, the spins remain coupled due to J_2 . In contrast, in the dimer picture substituting one zinc ion for a copper ion corresponds to a creation of one free spin.

Zinc doped samples of $\text{Ba}(\text{Cu}_{1-x}\text{Zn}_x)_2\text{V}_2\text{O}_8$ ($x=0.05, 0.1, 0.15, 0.2, 0.3$ and 0.4) were synthesized, however susceptibility measurements were only made for $x=0, 0.05$ and 0.1 . It is expected that susceptibility measurements on the samples with higher amount of doping will result in spin gap values that continue to show the same trend (Figure 6.1, weak dependence of the spin gap on doping amount). This will help confirm the conclusion in this work that the isolated dimer model is the most suitable for this system.

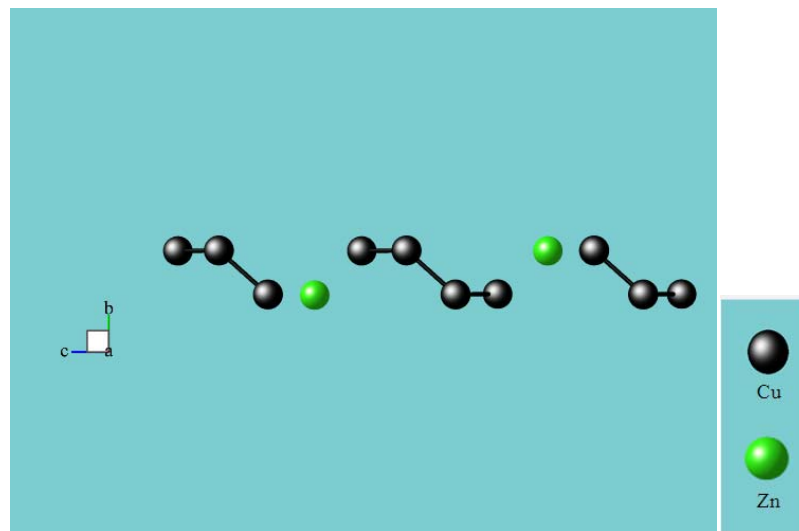


Figure 6.4 Alternating exchange model with zinc doping. Interdimer interaction will affect the excitation spectrum.

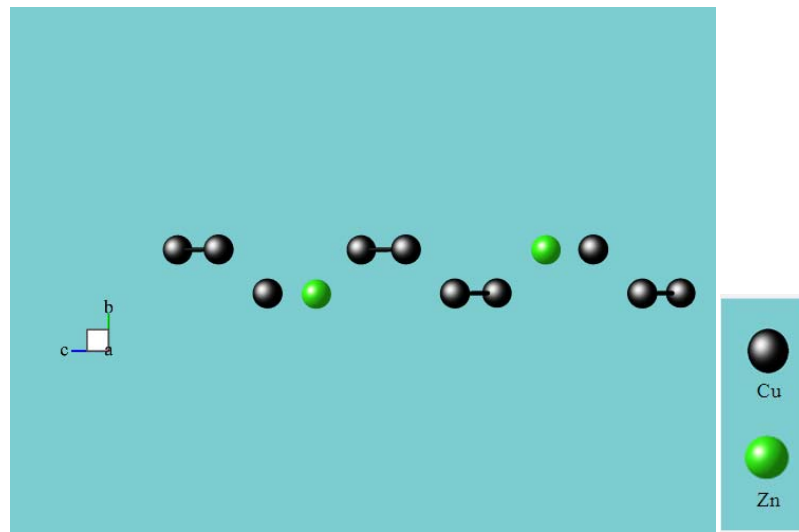


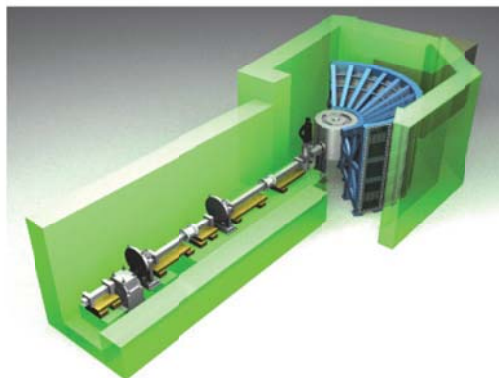
Figure 6.5 Isolated dimer model with zinc doping. The magnitude of the gap for each dimer is unaffected.

CHAPTER VII SUGGESTIONS

7.1 Inelastic neutron scattering

The following proposal was sent to Japan Proton Accelerator Research Complex (J-PARC) for the use of the 4SEASONS neutron spectrometer [Fig 7.1]. The proposal was not approved.

BL01: 4D Space Access Neutron Spectrometer—4SEASONS(四季)—



Specifications

Beamline	BL01
Moderator	Coupled
Neutron guides	Elliptically converging shape with $m = 3.2-4$ supermirrors
Incident energy	10–300 meV
Energy resolution	$\Delta E/E_i > 5\%$ FWHM at $E = 0$ when $\Delta t_{ch} = \Delta t_m$
Flight paths	Moderator-sample = 18.03 m, Sample-detector = 2.5 m
Fermi chopper	At 1.71 m upstream of the sample, rotating at 25–600 Hz, at 25-Hz intervals
Band definition choppers	Two disk choppers at 9 m and 12 m, rotating at 25 or 12.5 Hz Aperture = 77° (at 9 m) and 103° (at 12 m)
Background (T0) chopper	At 8.5 m, rotating in 25 or 50 Hz
Detectors	Position-sensitive ^3He tubes cylindrically arranged at 2.5 m from the sample position Horizontal coverage: -35° to 55° (-35° to 130° in the future) Vertical coverage: -25° to 27°

Figure 7.1 4SEASONS neutron spectrometer.

7.1.1 Proposal

Several studies about the origin of the spin gap in $\text{BaCu}_2\text{V}_2\text{O}_8$ were made by different groups by means of magnetic susceptibility [2-4] and heat capacity measurements [3], nuclear magnetic resonance (NMR) [5-7], and electronic structure calculations [2,8]. However there are inconsistencies in the suggested dominant exchange paths and alternation parameter [4]. These different studies find the gap in the range between $\Delta/k_B=230\text{K}$ and 470K depending on their methods and fit model (isolated dimer/ alternating exchange). So far no one has directly measured the gap using inelastic neutron scattering. At 4SEASONS, inelastic neutron scattering measurements on a polycrystalline samples of $\text{BaCu}_2\text{V}_2\text{O}_8$ would for the first time allow a direct measurement of the spin gap. An energy range of the spectrometer is most suitable for measuring the spin gap at $\sim 41\text{meV}$. The result can be used to determine the correct model for this system and the origin of the spin gap. Recently a measurement of the spin gap in the material $\text{NaTiSi}_2\text{O}_6$, which is a realization of a spin-Peierls system, was performed using neutron spectroscopy on a polycrystalline sample at ARCS in the Spallation Neutron Source (Oak Ridge National Laboratory, Oak Ridge, TN) and a spin gap of 53meV was directly measured [9]. We propose a similar measurement on our compound using 4SEASONS.

7.1.1.1 Method and time estimate of the beamtime

At 4SEASONS, we will perform the proposed measurements on a polycrystalline sample with a total mass of about 10g. The measurements will be conducted with the incident energy E_i about 100 meV, which should enable us to clearly observe the spin gap excitations with a reasonable counting time. We expect to find the gap around 41meV in accordance with our previous magnetic susceptibility study. In addition, we will take advantage of the spectrometer capacity of making simultaneous measurements at different E_i , which would help us to explore a large dynamic range, where unexpected spin dynamics may emerge. The sample will be cooled to base temperature using a closed-cycle cryostat, and we will complete the measurements at the base temperature and high temperatures for background subtraction. We request a total of 4 days of beamtime at 4SEASONS for these measurements. We note that we are trying to grow a large single crystal sample, which

so far has been unsuccessful. However, if a single crystal is obtained before the experiment we will do the measurement on a single crystal sample instead of the polycrystalline sample.

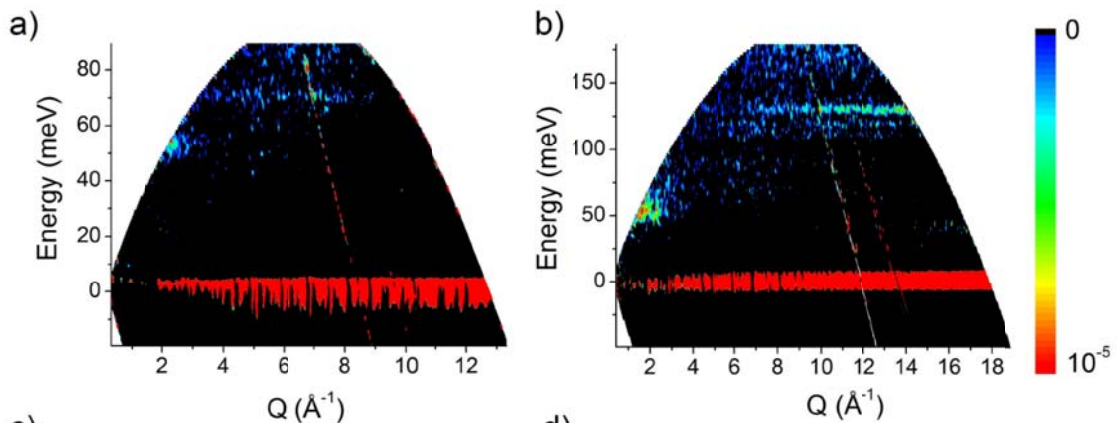


Figure 7.2 Direct measurement of the spin gap in $\text{NaTiSi}_2\text{O}_6$. Gap at $53\text{meV} \rightarrow \Delta/k_B=615\text{K}$.

7.1.1.2 List of relevant published literature and reference

- [1] I. Bose, *Curr. Sci.* 88, 62 (2005).
- [2] S. Sarita, Salunke et. al, *Phys. Rev. B* 77, 012410 (2008).
- [3] Z. He, T. Kyomen, and M. Itoh, *Phys. Rev. B* 69, 220407(R) (2004).
- [4] Z. He, T. Kyomen, and M. Itoh, *Journal of Magnetism and Magnetic Materials* 306 (2006).
- [5] C. S. Lue and B. X. Xie, *Phys. Rev. B* 72, 052409 (2005).
- [6] C. S. Lue and B. X. Xie, *Journal of Magnetism and Magnetic Materials* 310 (2007).
- [7] K. Ghoshray, B. Pahari, B. Bandyopadhyay, R. Sarkar, A. Ghoshray, *Phys. Rev. B* 71, 214401 (2005).
- [8] H.-J. Koo and M.-H. Whangbo, *Inorg. Chem.* 45, 4440 (2006).
- [9] H. J. Silverstein et al, *Phys. Rev. B* 90, 140402 (2014).
- [10] H. Sakuai, K. Yoshimura, K. Kosuge, *Phys. Soc. Jpn. Vol.* 71 (2002)

7.1.2 reviews

The following are the J-PARC committee comments.

Technical Review Report: They want to measure the powder sample at two temperatures (base T and higher T) with $E_i = 100$ meV. Although this compound is a spin half system, the measurements for two days are enough.

Referee 1 Comments: Investigation on one of interesting issues in low dimensional quantum magnetic systems. Experiment itself is promising. Therefore, it is worth doing in higher priority.

Referee 2 Comments: This proposal is on the spin excitations in the 1D alternating Heisenberg AF chain compound BaCu₂V₂O₈. There are several candidates for the gap origin for this compound, and to conclusively pin down the origin the inelastic neutron scattering is definitely necessary. This proposal seems rather old-fashioned, but low-dimensional quantum systems have always brought us unexpected something new, so I recommend this proposal to be performed.

Referee 3 Comments: Similar proposal on the same compound by using single crystal was submitted by different group in 2014B and it was accepted. I do not know what was going on that proposal, though. The present author prepared polycrystalline sample and I'm afraid that they may not obtain more meaningful data than the different group did in 2014B.

Referee 4 Comments: To determine the spin gap, inelastic neutron experiment using a powder sample is proposed. As stated, it would be nice if proposers can prepare single crystals. This would provide much information including magnitudes of the magnetic interactions. 10 g of powder samples sounds enough to conduct an experiment even at HRC, where the proposers can determine the gap value detailedly.

REFERENCES

1. Heisenberg, W. Z. Phys. 49, 619. (1928)
2. Dirac, P. A. M. Proc. Roy. Soc. (London) A123, 714. (1929)
3. W. Lenz: Z. Physik 21, 613 (1920); E. Ising: Z. Physik 31, 253 (1925)
4. H. Bethe: Z. Physik 71, 205 (1931)
5. W. Heisenberg: Z. Physik 49, 619 (1928)
6. M. Hase, I. Terasaki, K. Uchinokura: Phys. Rev. Lett. 70, 3651 (1993)
7. N.D. Mermin, H. Wagner: Phys. Rev. Lett. 17, 1133 (1966)
8. S. Coleman: Commun. Math. Phys. 31, 259 (1973)
9. Mourigal, M., Enderle, M., Klöpperpieper, A., Caux, J. S., Stunault, A., and Rønnow, H. M. (2013). Nature Physics 9(7), 435-441 (2013).
10. U. Schollwöck, J. Richter, D.J.J. Farnell, R.F. Bishop (Eds.), *Quantum Magnetism*, Lect.Notes Phys. 645 (Springer, Berlin Heidelberg 2004)
11. J. C. Bonner and M. E. Fisher, Phys. Rev. 135, A640 (1964).
12. S. Eggert, I. Affleck, and M. Takahashi, Phys. Rev. Lett. 73, 332 (1994).
13. M. Troyer, H. Tsunetsugu, and D. Würtz, Phys. Rev. B 50, 13 515 (1994).
14. D. C. Johnston, R. K. Kremer, M. Troyer, X. Wang, A. Klümper, S. L. Budko, A. F. Panchula, and P. C. Canfield, Phys. Rev. B61, 9558 (2000).
15. R. Vogt, Hk. Muller-Buschbaum, Z. Anorg. Allg. Chem.591 167 (1990).
16. Z. He, T. Kyomen, and M. Itoh, Phys. Rev. B 69, 220407(R) (2004).
17. Z. He, T. Kyomen, and M. Itoh, J. Magn. Magn. Mater. 306 (2006).
18. C. S. Lue and B. X. Xie, Phys. Rev. B 72, 052409 (2005).
19. H.-J. Koo and M.-H. Whangbo, Inorg. Chem. 45, 4440 (2006).
20. Sarita S. Salunke et. al., Phys. Rev. B, 77, 012410 (2008).
21. K. Ghoshray, B. Pahari, B. Bandyopadhyay. Phys. Rev. B.71.214401 (2005)
22. C. S. Lue, C. N. Kuo, D. S. Tasi, Y. K. Kuo. Phys. Rev. B.78.012406 (2008)
23. Hyun-Joo Koo. J. Inorg. Chem. 45 (2006)
24. H. Sakuai ,K Yoshimura, K. Kosuge. J. Phys. Soc. Jpn. Vol. 71 (2002).

25. C. S. Lue and B. X. Xie, *J. Magn. Magn. Mater.* 310 (2007).
26. Z. He, T. Kyomen, and M. Itoh, *J. of Cryst. Growth* 274 (2005).
27. I. Bose, *Curr. Sci.* 88, 62 (2005).
28. <http://www.crystallography.net/cod/2002467.html>

BIOGRAPHY

NAME	Mr. Yuval Shilon
DATE OF BIRTH	5 March 1984
PLACE OF BIRTH	Haifa, Israel
INSTITUTIONS ATTENDED	Ben Gurion University, 2008-2012: Bachelor of science (Physics) Mahidol University, 2012-2015: Master of science (Physics)
SCHOLARSHIP RECEIVED	Faculty of science, Mahidol university
HOME ADDRESS	95 Charansanitwong soi 70/2, Bang plad Bang Plad, Bangkok 10700 Tel. 0886725908 E-mail : yuval256@gmail.com
PUBLICATION / PRESENTATION	EFFECTS OF Zn DOPING ON THE SPIN GAP CHARACTERISTICS OF THE SPIN 1/2 COMPOUND $\text{BaCu}_2\text{V}_2\text{O}_8$ Stt40 International Conference 2014, Khon Kean, Thailand (oral presentation)